frontiers | Frontiers in Earth Science

TYPE Original Research
PUBLISHED 08 February 2024
DOI 10.3389/feart.2024.1342969

Check for updates

OPEN ACCESS

EDITED BY
Paolo Capuano,
University of Salerno, Italy

REVIEWED BY
Muhsan Ehsan,
Bahria University, Pakistan
Hua-Wen Cao,
Chengdu University of Technology, China

*CORRESPONDENCE
Guiling Wang,
✉ ihegwangguiling@sina.com

RECEIVED 22 November 2023
ACCEPTED 08 January 2024
PUBLISHED 08 February 2024

CITATION
Liao Y, Wang G, Xi Y, Gan H, Yan X, Yu M, Zhang W and Zhao Z (2024), Petrogenesis of high heat producing granites and their contribution to geothermal resource in the Huangshadong geothermal field, South China. *Front. Earth Sci.* 12:1342969.
doi: 10.3389/feart.2024.1342969

COPYRIGHT
© 2024 Liao, Wang, Xi, Gan, Yan, Yu, Zhang and Zhao. This is an open-access article distributed under the terms of the Creative Commons Attribution License (CC BY). The use, distribution or reproduction in other forums is permitted, provided the original author(s) and the copyright owner(s) are credited and that the original publication in this journal is cited, in accordance with accepted academic practice. No use, distribution or reproduction is permitted which does not comply with these terms.

Petrogenesis of high heat producing granites and their contribution to geothermal resource in the Huangshadong geothermal field, South China

Yuzhong Liao[1,2], Guiling Wang[1,2]*, Yufei Xi[1,2], Haonan Gan[1,2], Xiaoxue Yan[1,2], Mingxiao Yu[1,2], Wei Zhang[1,2] and Zirui Zhao[1,2]

[1]Institute of Hydrogeology and Environmental Geology, Chinese Academy of Geological Sciences, Shijiazhuang, China, [2]Technology Innovation Center for Geothermal & Hot Dry Rock Exploration and Development, Ministry of Natural Resources, Shijiazhuang, China

The Huangshadong geothermal field (HGF), situated in the contact zone between Mesozoic granites and NE-striking dominant faults in South China, has great geothermal potential. Petrogenesis of reservoir rock plays an important role in understandings its genetic mechanism and assessing geothermal potential. However, due to the lack of rock sample at depth collected from the geothermal reservoir, the petrogenesis of granites in the geothermal reservoirs of the HGF, remains an enigma. This study elucidated the petrogenetic characteristics of these granites sampled directly from geothermal reservoir at the depth of ~3,000 km and their geothermal implications through zircon U-Pb dating, geochemical analysis, and Hf isotopic analysis. The zircon U-Pb ages indicate that the magmatism evolution of HGF contains three eras, namely, Cretaceous (135 ± 4 to 143.6 ± 2.8 Ma), Jurassic (152.7 ± 2.7 to 176.7 ± 1.8 Ma), and Permian granites (251 ± 9.1 to 251 ± 5 Ma) from the youngest to oldest. The reservoir granites were emplaced during the latest stage of Cretaceous intrusion, as indicated by the zircon U-Pb ages (135 ± 4 Ma and 135.3 ± 2.4 Ma) of rock samples from the deep part of well HR-1. These Cretaceous rocks are highly fractionated I-type granites, featuring high SiO_2, K_2O, and Na_2O contents, high Rb/Sr ratios, low Zr/Hf, Nb/Ta, and Th/U ratios, and A/CNK values of 1.05–1.13. Compared to other Cretaceous granites outcropping on the margin of the HGF, these granites have undergone the strongest fractional differentiation. The Cretaceous granites in the HGF are high-heat-producing rocks (>5 μW/m^3), with an average heat production rate of 6.63 μW/m^3. Notably, the Cretaceous reservoir granites (as reservoir rocks) serve as an important heat source for the formation of geothermal resources in the HGF. In addition, the zircon Hf isotopic composition indicates that the reservoir Cretaceous granites originated from Meso-to Paleo-Proterozoic lower crustal materials (T_{DM2}: 1,385 to 1907 Ma).

KEYWORDS

high-heat-producing granite, Huangshadong geothermal field, cretaceous granite, highly fractionated granite, heat source

1 Introduction

Geothermal resources have attracted wide attention worldwide owing to their clean and sustainable nature (Tester et al., 2006; Lin et al., 2016; Lu, 2018; Lin et al., 2022; Ma et al., 2022; Chen et al., 2023). The geothermal energy utilized directly was up to 107,727 MWt in 2020, increasing by 52% since 2015 (Lu, 2018; Lund and Toth, 2021). The petrological characteristics of geothermal reservoir rocks serve as key parameters used to evaluate the geothermal potential and analyze the genesis of geothermal resources, especially for a granite-hosted geothermal system (Zhang et al., 2022; Alqahtani et al., 2023a; Alqahtani et al., 2023b; Ullah et al., 2023; Wang et al., 2023).

The heat for thermal anomalies originates from the radioactive decay of heat-producing elements (U, Th, and K) (Hasterok and Chapman, 2011; Wang et al., 2023). The upper crust has average U, Th, and K_2O contents of 2.7 ppm, 10.5 ppm, and 2.8%, respectively, with a radioactive heat production rate of 1.75 $\mu W/m^3$ (Kemp and Hawkesworth, 2003; Kromkhun, 2010). In contrast, the granites are relatively rich in incompatible elements such as U, Th, and K, with average contents of 3.9 ppm, 16 ppm, and 3.6%, respectively. This enrichment results in a radioactive heat production rate of 2.53 $\mu W/m^3$. Due to their incompatibility, these heat-producing elements are usually concentrated in the shallow crust, diminishing with depth. The granitic upper crust has depths of mostly 10–20 km, and its radioactive heat production contributes surface heat flow of 10–20 $\mu W/m^2$, which accounts for 50% of the surface heat in the stable continental crust (Artemieva and Thybo, 2013). High-heat-producing granites, with radioactive heat production rates >5 $\mu W/m^3$, play a critical role in the formation of geothermal resources (Marshall, 2014; Artemieva et al., 2017). For instance, the Cooper Basin, which is subjected to the most recent intrusion of Carboniferous-Permian granodiorites rather than present-day magmatic events (Big Lake Suite, 310–327 Ma; (Marshall, 2014), records the terrestrial heat flow values measuring >100 mW/m^2. However, the minimum heat flow value is only 33 mW/m^2, which occurs at the edge of the rock mass in a borehole. This finding indicates that the temperature anomalies are primarily derived from the high-heat-producing granites in the basement, which have a maximum radioactive heat production rate of up to 10 $\mu W/m^3$ (Roth and Littke, 2022).

A large quantity of Mesozoic granites in South China are genetically related to geothermal energy (Lin et al., 2016; Qiu et al., 2018; Liu et al., 2021; Lin et al., 2022; Lin et al., 2023; Pang and Huang, 2023). The granites in South China have an average heat

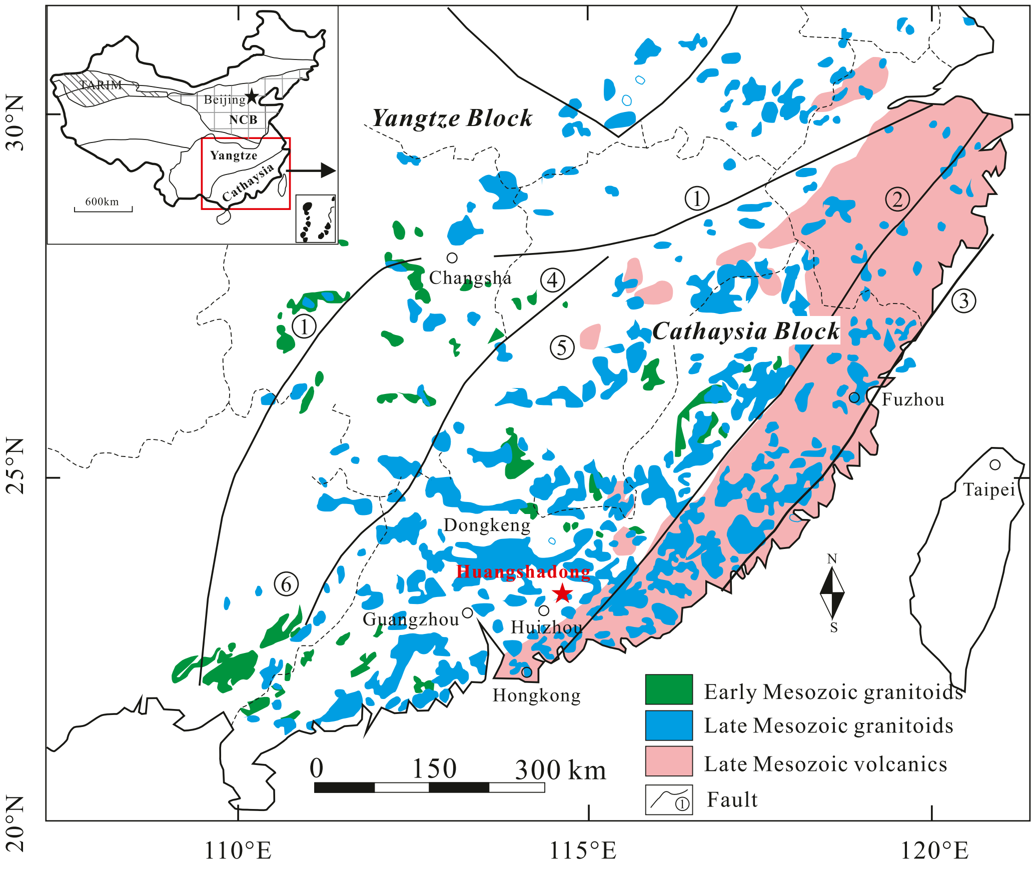

FIGURE 1
Geological map of the Nanling Range, South China (modified after Chen et al. (2014), copyright@Elsevier, 2016). Faults: (1) Jiangshan-Shaoxing-Pingxiang Fault; (2) Zhenghe-Dapu Fault; (3) Changle-NanaoFault; (4) Chenzhou-Linwu Fault; (5) Changlin-Guangchang buried Fault; (6) Wuzhou-Sihui buried Fault. NCB: North China Craton. TARIM: Tarim Basin.

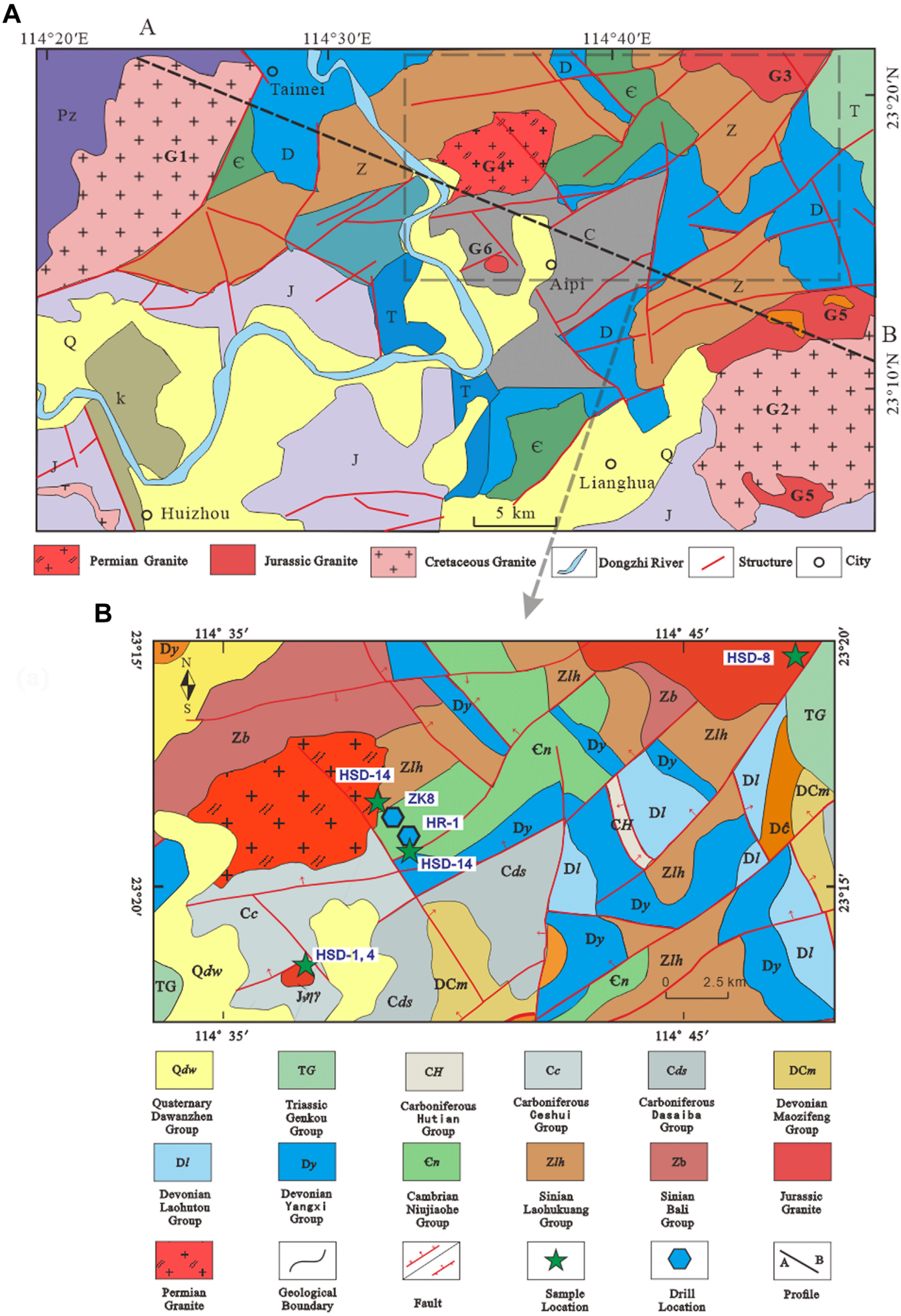

FIGURE 2
(A) Geological sketch maps of the Huangshadong geothermal field (modified after Xiao et al., 2019). Pz = Paleozoic; Z = Sinian; Є = Cambrian; D = Devonian; C = Carboniferous; T = Triassic; J = Jurassic; K = Cretaceous; Q = Quaternary. **(B)** Location of geothermal wells and samples in the Huangshadong geothermal field (modified after Zuo et al., 2018).

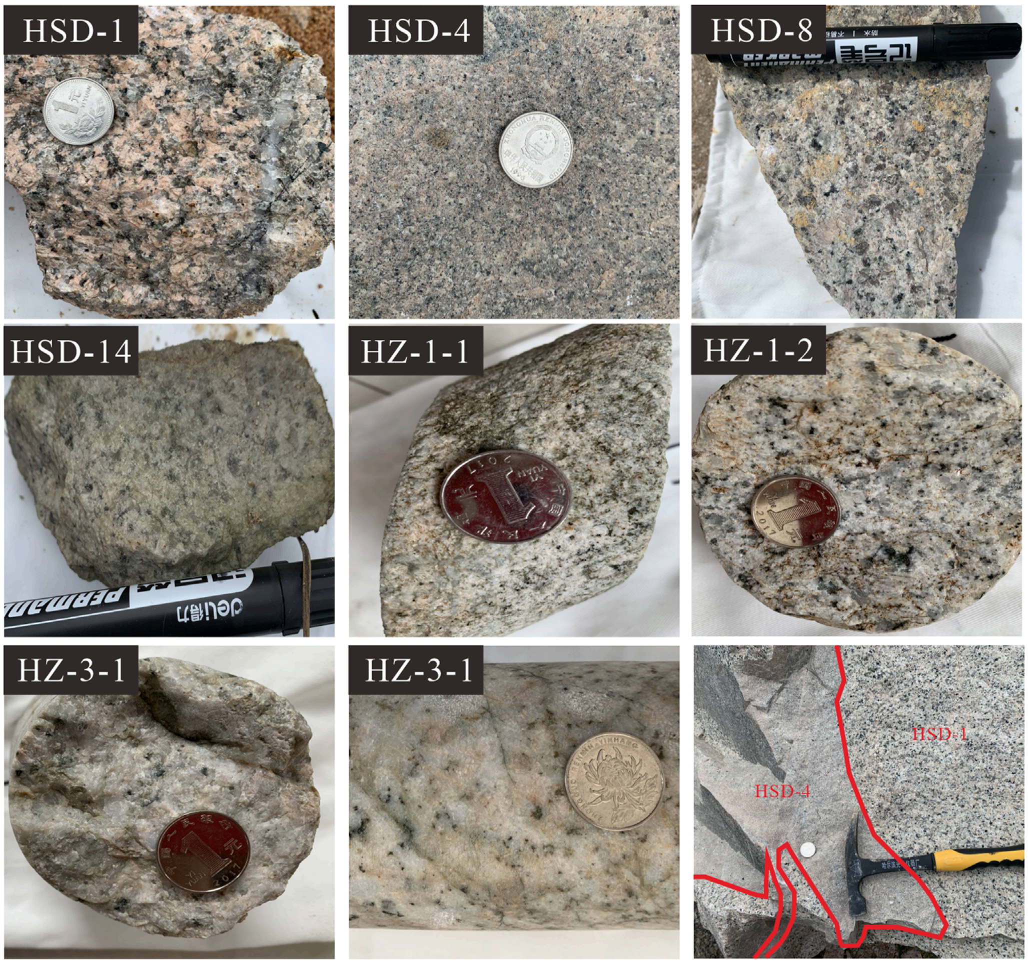

FIGURE 3
Photographs of the Huangshadong granites.

TABLE 1 Location of rock samples in the study area.

Sample	Longitude	Latitude	Depth (m)	Elevation (m)	Property
HSD-1	114°37′	23°13′		64	surface outcrop
HSD-4	114°37′	23°14′		82	surface outcrop
HSD-8	114°47′	23°20′		78	surface outcrop
HSD-14	114°38′	23°17′		91	surface outcrop
HZ-1	114°38′	23°16′	1831		geothermal well
HZ-3-1	114°38′	23°16′	2,637		geothermal well
HZ-3-2	114°38′	23°16′	2,702		geothermal well

production rate of 3 $\mu W/m^3$ (Zhao and Luo, 1995). Among them, granites in Guangdong Province have an average heat production rate of 5.7 $\mu W/m^3$, classified as high-heat-producing rocks. Many thermal springs are distributed in the HGF, with temperatures of 56–63.7°C and a flow rate of 0.38 L/s (Lin et al., 2016). Geothermal wells ZK 8 and HR-1 revealed high temperatures of 118.3°C and 127.5°C, respectively at depths of 591.5 m and 2,900 m (Xiao et al., 2019; Li et al., 2020a).

Previous studies of granites in the HGF focus on their regional petrogeological characteristics, subjected to rock samples collected from outcrops or shallow buried plutons (~300 m below the surface; Xiao et al., 2019). Most of the samples were collected from outcrops

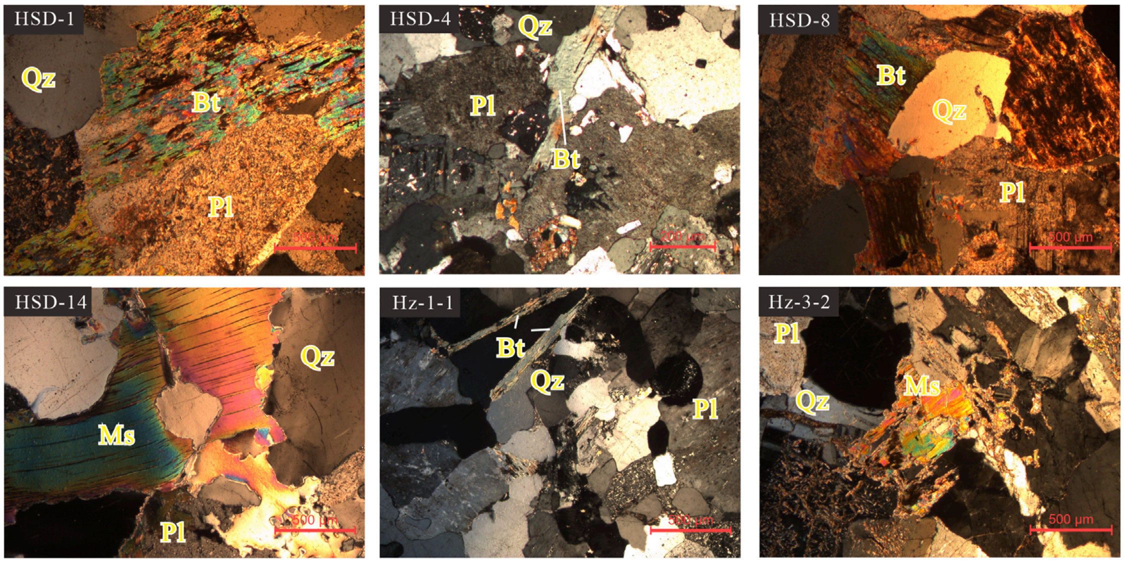

FIGURE 4
Microscope photographs of the granites in the Huangshadong geothermal field. Abbreviations: Qz = Quartz, Pl = Plagioclase, Bt = Biotite, Ms = Muscovite.

FIGURE 5
Cathodoluminescence images of zircons with corresponding $^{206}Pb/^{238}U$ ages for the samples from the Huangshadong geothermal field.

at a great distance from HGF (G1, G2, G3, and G5 in Figure 2). As a result, the petrogenesis of geothermal reservoir granites buried at depth in the areas where a bunch of hot springs are exposed (locations of wells HR-1 and ZK8), as well as the genetic relationship between them and geothermal energy, remains unclear. This study conducted geochronological, geochemical, and Hf isotopic analyses of granites in the HGF (especially the reservoir granites dredged by HR-1 from the depth of ~3,000 km), aiming to promote the understanding of the genetic relationship between the geothermal resources and high-heat-producing granites.

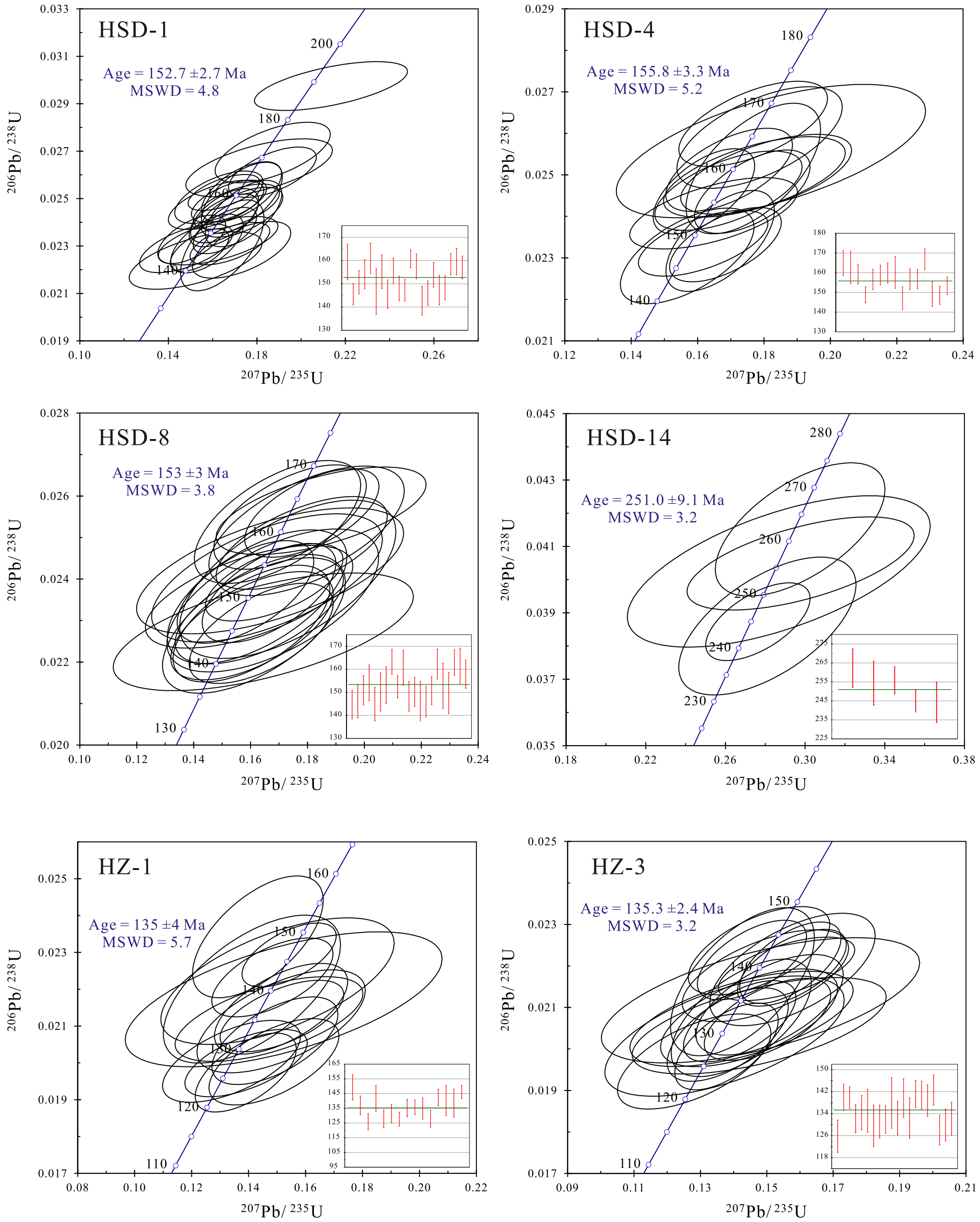

FIGURE 6
Zircon LA-ICP-MS U–Pb concordia diagrams for the Huangshadong geothermal field. Data processing was carried out using concordia intercept ages on the Tera-Wasserburg plot utilizing ISOPLOT.

2 Geological setting

The South China Block (SCB) was formed by the amalgamation of the Yangtze Block in the northwest and the Cathaysia Block in the southeast during 1.0–0.9 Ga (Zhou et al., 2006) (Figure 1). The NE-striking Qinzhou Bay - Hangzhou Bay (Qin-Hang) suture zone between the latter two blocks was reactivated during the Middle-Late Mesozoic, leading to the formation of numerous plutons (Li et al., 2009; Mao et al., 2011; Hu et al., 2017). Regionally, there are six primary faults striking NE to NEE, namely, the Jiangshan-Shaoxing-Pingxiang, Zhenghe-Dapu, Changle-Nan'ao, Chenzhou-Linwu faults, and the Changlin-Guangchang and the Wuzhou-Sihui concealed faults. The HGF is located approximately 20 km northeast of Huizhou City, Guangdong Province (Figure 1).

The stratigraphy in the HGF consists primarily of Sinian and Cambrian metasedimentary strata, as well as Devonian, Carboniferous, Triassic, and Quaternary sedimentary strata (Figure 2). The Sinian metasedimentary strata contain two formations, namely, Laohukuang (Zlh, 725 m thick) and Bali

TABLE 2 Zircon U-Pb dating results of the granites in the Huangshadong geothermal field.

Spot	$^{208}Pb/^{232}Th$	1σ	$^{232}Th/^{238}U$	$^{207}Pb/^{206}Pb$	1σ	$^{207}Pb/^{235}U$	1σ	$^{206}Pb/^{238}U$	1σ	Th	U	Th/U	Ti	$T_{ti\text{-}in\text{-}zircon}$
Sample HZ-1	135±4 Ma													
HZ-1–2	0.0073	0.0004	0.52	120	218	136	8	149	4	201	385	0.52	3.06	646
HZ-1–4	0.0074	0.0003	0.51	261	168	143	8	137	3	147	286	0.51	4.60	678
HZ-1–7	0.0063	0.0002	0.49	243	137	132	6	126	3	273	554	0.49	2.50	630
HZ-1–8	0.0073	0.0005	0.55	302	287	142	15	142	4	58	105	0.56	6.92	712
HZ-1–9	0.0064	0.0002	0.81	394	165	141	8	128	3	384	479	0.80	15.03	786
HZ-1–12	0.0064	0.0003	0.51	309	158	141	8	131	3	241	463	0.52	1.91	611
HZ-1–13	0.0064	0.0002	0.71	217	158	132	8	128	2	349	488	0.72	3.98	666
HZ-1–16	0.0094	0.0005	0.57	213	284	139	12	135	3	138	238	0.58	5.93	699
HZ-1–17	0.0070	0.0003	0.48	257	156	143	8	136	3	224	453	0.49	2.10	618
HZ-1–18	0.0070	0.0003	0.79	391	216	143	11	135	4	127	160	0.79	10.39	750
HZ-1–19	0.0068	0.0004	0.52	83	215	128	9	128	3	122	237	0.52	3.19	649
HZ-1–21	0.0073	0.0003	0.64	78	143	140	8	142	3	241	371	0.65	8.46	730
HZ-1–23	0.0065	0.0004	0.57	65	278	134	11	140	5	116	204	0.57	10.23	748
HZ-1–24	0.0068	0.0005	0.66	234	372	144	20	139	5	58	84	0.69	8.76	734
HZ-1–25	0.0068	0.0002	0.51	106	111	146	6	146	2	361	723	0.50	2.55	632
Sample HZ-3	135.3±2.4 Ma													
HZ-3–1	0.0058	0.0003	0.61	61	200	122	8	126	3	217	360	0.60	4.73	680
HZ-3–5	0.0079	0.0002	0.34	288	98	149	6	140	2	483	1,445	0.33	3.94	665
HZ-3–6	0.0098	0.0003	0.51	267	128	147	7	140	2	825	1,626	0.51	3.77	662
HZ-3–7	0.0073	0.0003	0.43	312	125	142	7	132	3	308	728	0.42	2.99	644
HZ-3–8	0.0073	0.0003	0.47	283	159	143	8	134	3	192	406	0.47	1.85	609
HZ-3–9	0.0063	0.0004	0.57	229	587	140	17	135	4	66	116	0.57	8.95	736

(Continued on the following page)

TABLE 2 (*Continued*) Zircon U-Pb dating results of the granites in the Huangshadong geothermal field.

Spot	$^{208}Pb/^{232}Th$	1σ	$^{232}Th/^{238}U$	$^{207}Pb/^{206}Pb$	1σ	$^{207}Pb/^{235}U$	1σ	$^{206}Pb/^{238}U$	1σ	Th	U	Th/U	Ti	$T_{ti\text{-}in\text{-}zircon}$
HZ-3–10	0.0120	0.0012	0.42	149	338	131	13	130	4	95	232	0.41	4.38	674
HZ-3–11	0.0076	0.0004	0.72	290	264	140	13	131	3	208	269	0.77	3.63	659
HZ-3–12	0.0065	0.0002	0.50	143	120	135	6	132	3	642	1,242	0.52	1.79	606
HZ-3–13	0.0076	0.0004	0.50	117	181	135	8	138	5	256	485	0.53	1.23	581
HZ-3–14	0.0061	0.0002	0.93	221	237	137	9	132	3	318	331	0.96	4.49	676
HZ-3–15	0.0078	0.0004	0.59	435	211	149	9	140	3	124	211	0.59	8.30	729
HZ-3–17	0.0065	0.0004	0.54	332	199	135	8	132	4	153	283	0.54	4.17	670
HZ-3–18	0.0072	0.0002	0.41	32	115	138	6	141	2	392	961	0.41	2.98	644
HZ-3–19	0.0072	0.0003	0.40	233	102	148	5	141	3	579	1,433	0.40	2.93	642
HZ-3–20	0.0076	0.0003	0.43	188	172	142	9	139	3	232	549	0.42	3.55	657
HZ-3–22	0.0072	0.0003	0.61	83	148	140	8	143	3	200	320	0.63	2.88	641
HZ-3–23	0.0069	0.0003	0.40	189	121	131	6	128	3	322	823	0.39	2.18	620
HZ-3–24	0.0059	0.0003	0.43	143	133	131	7	130	3	319	749	0.43	2.78	638
HZ-3–25	0.0153	0.0012	0.47	188	248	135	12	132	3	358	775	0.46	0.50	526
Sample HSD-1	152.7±2.7 Ma													
HSD-1–1	0.0069	0.0003	0.54	214	115	162	6	159	4	622	1,072	0.58	2.20	621
HSD-1–2	0.0071	0.0002	0.29	112	86	146	5	145	2	886	3,028	0.29	1.23	581
HSD-1–3	0.0076	0.0003	0.41	228	94	156	5	151	3	715	1733	0.41	1.08	572
HSD-1–5	0.0075	0.0003	0.32	164	100	155	6	154	3	536	1,674	0.32	6.50	707
HSD-1–6	0.0082	0.0003	0.65	163	104	162	6	161	3	743	1,113	0.67	2.66	635

(Continued on the following page)

TABLE 2 (*Continued*) (*Continued*) Zircon U-Pb dating results of the granites in the Huangshadong geothermal field.

Spot	$^{208}Pb/^{232}Th$	1σ	$^{232}Th/^{238}U$	$^{207}Pb/^{206}Pb$	1σ	$^{207}Pb/^{235}U$	1σ	$^{206}Pb/^{238}U$	1σ	Th	U	Th/U	Ti	$T_{ti\text{-}in\text{-}zircon}$
HSD-1–7	0.0098	0.0003	0.59	275	136	155	7	147	5	582	978	0.60	3.12	647
HSD-1–8	0.0082	0.0003	0.43	303	106	163	6	155	4	719	1,679	0.43	1.48	593
HSD-1–10	0.0078	0.0003	0.43	405	123	162	8	146	3	309	748	0.41	1.11	574
HSD-1–11	0.0078	0.0003	0.37	237	104	162	7	156	3	351	982	0.36	1.77	606
HSD-1–12	0.0086	0.0003	0.45	230	165	153	9	148	3	237	560	0.42	3.09	646
HSD-1–13	0.0074	0.0003	0.41	301	105	157	6	147	2	373	950	0.39	0.22	481
HSD-1–14	0.0081	0.0003	0.39	35	96	155	6	161	2	459	1,205	0.38	1.68	602
HSD-1–15	0.0083	0.0003	0.40	55	144	152	8	157	3	234	585	0.40	3.46	655
HSD-1–16	0.0095	0.0004	0.73	165	252	144	10	143	3	576	816	0.71	4.58	677
HSD-1–17	0.0076	0.0003	0.38	40	160	140	8	146	3	235	630	0.37	2.83	640
HSD-1–19	0.0071	0.0002	0.43	159	87	155	5	154	3	702	1708	0.41	2.80	639
HSD-1–20	0.0069	0.0002	0.40	161	97	148	6	147	3	607	1,538	0.39	0.83	556
HSD-1–21	0.0068	0.0003	0.31	33	101	142	6	148	3	448	1,495	0.30	2.06	616
HSD-1–23	0.0071	0.0002	0.54	118	99	157	6	158	2	706	1,319	0.54	2.48	630
HSD-1–24	0.0073	0.0003	0.50	79	137	153	7	160	3	240	477	0.50	4.13	669
HSD-1–25	0.0069	0.0002	0.42	208	122	160	7	157	2	318	764	0.42	2.01	615
Sample HSD-4	155.8±3.3 Ma													
HSD-4–2	0.0079	0.0003	0.48	196	150	167	9	165	3	295	617	0.48	2.94	643
HSD-4–4	0.0082	0.0005	0.82	270	325	170	16	163	4	97	118	0.82	12.55	768
HSD-4–5	0.0101	0.0004	0.31	302	132	169	9	159	2	397	1,281	0.31	0.00	0
HSD-4–7	0.0093	0.0003	0.44	205	120	152	7	149	2	631	1,405	0.45	2.52	631
HSD-4–11	0.0086	0.0003	0.41	272	100	165	6	157	3	476	1,183	0.40	3.51	656
HSD-4–12	0.0082	0.0003	0.48	263	160	166	9	159	2	272	556	0.49	4.11	669

(Continued on the following page)

TABLE 2 (*Continued*) (*Continued*) (*Continued*) Zircon U-Pb dating results of the granites in the Huangshadong geothermal field.

Spot	^{208}Pb/^{232}Th	1σ	^{232}Th/^{238}U	^{207}Pb/^{206}Pb	1σ	^{207}Pb/^{235}U	1σ	^{206}Pb/^{238}U	1σ	Th	U	Th/U	Ti	$T_{ti\text{-}in\text{-}zircon}$
HSD-4–14	0.0072	0.0002	0.64	120	−84	159	7	160	3	582	847	0.69	4.28	672
HSD-4–15	0.0088	0.0003	0.38	240	102	165	7	160	4	546	1,394	0.39	0.20	475
HSD-4–16	0.0075	0.0003	0.61	200	133	148	7	147	3	354	593	0.60	2.39	627
HSD-4–17	0.0077	0.0002	0.46	35	89	152	5	157	3	697	1,486	0.47	2.19	621
HSD-4–19	0.0077	0.0003	0.56	189	129	159	8	157	2	452	821	0.55	2.43	628
HSD-4–20	0.0080	0.0003	0.69	106	128	165	8	167	3	496	682	0.73	5.42	692
HSD-4–22	0.0080	0.0003	0.44	271	93	157	6	149	3	916	2016	0.45	10.12	747
HSD-4–23	0.0079	0.0003	0.33	272	93	158	6	149	2	870	2,637	0.33	0.00	0
HSD-4–25	0.0124	0.0004	0.37	179	147	155	8	153	2	460	1,211	0.38	3.83	663
Sample HSD-8	153±3 Ma													
HSD-8–1	0.0084	0.0004	0.38	300	165	154	9	145	3	99	249	0.40	4.40	674
HSD-8–2	0.0075	0.0004	0.38	220	180	151	10	146	4	86	229	0.38	5.71	696
HSD-8–3	0.0076	0.0003	0.80	128	170	149	9	151	3	180	225	0.80	3.79	662
HSD-8–4	0.0133	0.0006	0.47	196	352	157	16	154	4	199	401	0.50	14.21	780
HSD-8–7	0.0136	0.0007	0.47	307	280	155	17	145	4	113	229	0.49	4.65	679
HSD-8–8	0.0095	0.0004	0.48	192	218	153	11	150	4	116	225	0.52	5.44	692
HSD-8–9	0.0100	0.0005	0.41	197	264	156	14	153	4	103	243	0.42	5.79	697
HSD-8–11	0.0165	0.0007	0.30	297	164	172	12	163	3	230	727	0.32	5.94	699
HSD-8–12	0.0078	0.0003	0.49	228	146	158	9	152	2	237	451	0.53	5.41	691
HSD-8–13	0.0084	0.0004	0.49	270	206	168	12	161	4	81	166	0.49	4.57	677
HSD-8–15	0.0073	0.0004	0.74	237	213	153	10	148	3	171	226	0.76	7.01	714
HSD-8–16	0.0073	0.0004	0.62	152	233	150	13	150	3	96	150	0.64	7.63	721
HSD-8–17	0.0073	0.0004	0.49	300	218	152	11	146	4	87	175	0.49	6.93	713

(Continued on the following page)

TABLE 2 (*Continued*) (*Continued*) (*Continued*) (*Continued*) Zircon U-Pb dating results of the granites in the Huangshadong geothermal field.

Spot	$^{208}Pb/^{232}Th$	1σ	$^{232}Th/^{238}U$	$^{207}Pb/^{206}Pb$	1σ	$^{207}Pb/^{235}U$	1σ	$^{206}Pb/^{238}U$	1σ	Th	U	Th/U	Ti	$T_{ti\text{-}in\text{-}zircon}$
HSD-8–18	0.0110	0.0006	0.51	394	217	151	10	146	3	114	221	0.51	3.61	658
HSD-8–19	0.0077	0.0004	0.45	302	148	156	8	151	3	221	474	0.47	3.31	652
HSD-8–20	0.0078	0.0003	0.54	191	181	163	9	162	3	123	223	0.55	2.99	644
HSD-8–21	0.0079	0.0004	0.74	472	241	162	13	153	5	106	137	0.77	6.93	713
HSD-8–22	0.0077	0.0004	0.56	769	372	158	13	150	4	91	161	0.57	5.76	697
HSD-8–23	0.0077	0.0003	0.43	250	127	169	8	163	3	209	484	0.43	1.95	612
HSD-8–24	0.0065	0.0004	0.38	43	178	159	10	162	4	74	189	0.39	4.56	677
HSD-8–25	0.0089	0.0004	0.50	288	184	166	10	158	3	138	269	0.51	5.01	685
Sample HSD-14	251±9.1 Ma													
HSD-14.3	0.0129	0.0005	0.74	280	146	264	14	262	5	170	225	0.75	14.02	779
HSD-14.4	0.0141	0.0007	0.81	272	203	256	24	254	6	153	178	0.86	14.30	781
HSD-14.6	0.0168	0.0006	0.55	394	213	265	18	256	4	560	967	0.58	12.34	766
HSD-14.8	0.0128	0.0004	0.54	254	91	248	9	245	3	449	834	0.54	6.02	700
HSD-14–15	0.0151	0.0005	0.62	321	155	252	14	244	5	460	753	0.61	4.95	684

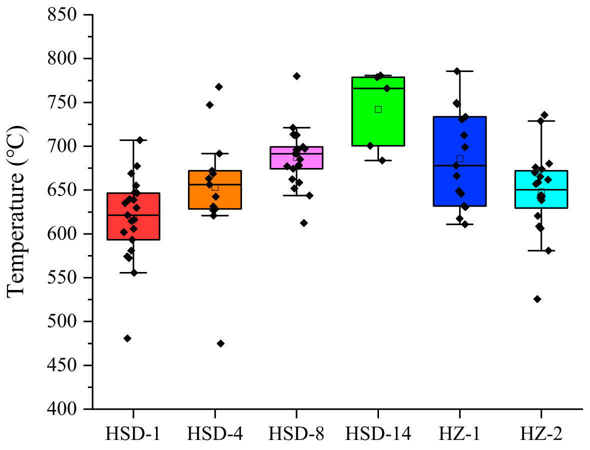

FIGURE 7
The Ti-in-zircon temperatures of the granites in the Huangshadong geothermal field.

(Zb, >500 m thick). The former is located in the eastern part of this gas field, comprising metasandstones and slates. In contrast, the latter is present in the northwestern part of the study area, consisting of metasandstones interbedded with slates. The Cambrian metasedimentary strata (Єn, 600 m thick) comprise metasandstones occasionally interbedded with phyllites. The Devonian sedimentary strata include the Yangxi (Dy, 370–750 m thick), Laohutou (Dl, 470–620 m thick), and Maozifeng (DCm, 65–410 m thick) formations. They occur in the southeastern part, comprising conglomerates, sandstones, and mudstones. The Carboniferous sedimentary strata are mainly present in the southwestern parts, consisting of three formations, namely, Dasaiba (Cds, 340–400 m thick), Ceshui (Cc, 300–400 m thick), and Hutian (CH, >150 m thick). Among them, the Dasaiba and Ceshui formations comprise quartz sandstones and slates, while the Hutian Formation is composed of limestones and dolomites. The Triassic Genkou Group (TG >1,250 m thick), which consists of conglomerates, sandstones, and mudstones, is found at the eastern and western edges of the HGF. The Quaternary sedimentary strata (Qdw, 10–25 m thick), primarily comprising clay, are distributed in the southwestern part.

Spatially, thermal springs in Guangdong Province are closely associated with the outcrops of intrusions (especially Yanshanian intrusions), mostly found in the contact zone between intrusions (granite complex) and host rocks (Xiao et al., 2019).

Granite complex in the HGF comprising three parts (Figure 2): 1) Cretaceous granite, dominant geothermal reservoir rock; 2) Jurassic granite, occurring in the northeastern part; 3) Permian granites exposed only in the central part. Geothermal surface manifestations occur in the contact zone between the Permian granites and the Cambrian metasedimentary rocks. Cretaceous granites were excavated at a depth of about 300 m by well ZK8 (Xiao et al., 2019), and concealed granites were revealed at a depth of 1,560 m by geothermal well HR-1 (Li et al., 2020a).

3 Sampling and petrography

Seven granite samples, namely, HSD-1, HSD-4, HSD-8, HSD-14, HZ-1-1, HZ-3-1, and HZ-3-2), were collected from the HGF for dating and geochemical analysis (Figure 3; Table 1). Each sample was 5–10 kg in weight. Samples HSD-1, HSD-4, HSD-8, and HSD-14 were taken from granite outcrops (Figures 2, 3). Among them, samples HSD-1 and HSD-4 were fresh massive rocks obtained from a strip pit in the southwestern part of the HGF, while sample HSD-8 was gathered from the northeastern part. Samples HSD-1 and HSD-8 were medium-to coarse-grained equigranular biotite granites, and sample HSD-4 consisted of fine-grained equigranular biotite granites. Sample HSD-14 was collected from the two-mica granite outcrops near geothermal well HR-1, with its weathered parts chipped off using a hammer. Samples HZ-1, HZ-3-1, and HZ-3-2 were collected at depths of 1831 m, 2,637 m, and 2,702 m, respectively in well HR-1 (Figure 3).

Fresh field samples were cut into blocks of ~45×25×15 mm using a diamond blade. Afterward, they were planed and then mounted on a 28×48 mm standard petrographic slide using epoxy. The thin sections measured 30 μm in thickness after being polished with abrasive powder. To identify the mineralogy and texture of rocks, the polished thin sections were examined under a binocular microscope and a Leica DM2700P polarization microscope at the Institute of Hydrogeology and Environmental Geology under the Chinese Academy of Geological Sciences.

TABLE 3 Ti-in-zircon temperatures of the igneous rocks in the Huangshadong geothermal field.

	T_{Ti} (°C)	T_{Ti} (°C)	T_{Ti} (°C)	T_{Ti} (°C)	T_{Ti} (°C)	T_{Ti} (°C)
Sample	HZ-1	HZ-3	HSD-1	HSD-4	HSD-8	HSD-14
Num	15	20	21	13	21	5
Minimum	611	526	481	475	612	684
Maximum	786	736	707	768	780	781
Median	678	650	621	656	691	766
Average	686	648	617	653	687	742

Note: T_{Ti}, denotes the Ti-in-zircon temperature; Num denotes the amount of temperature data.

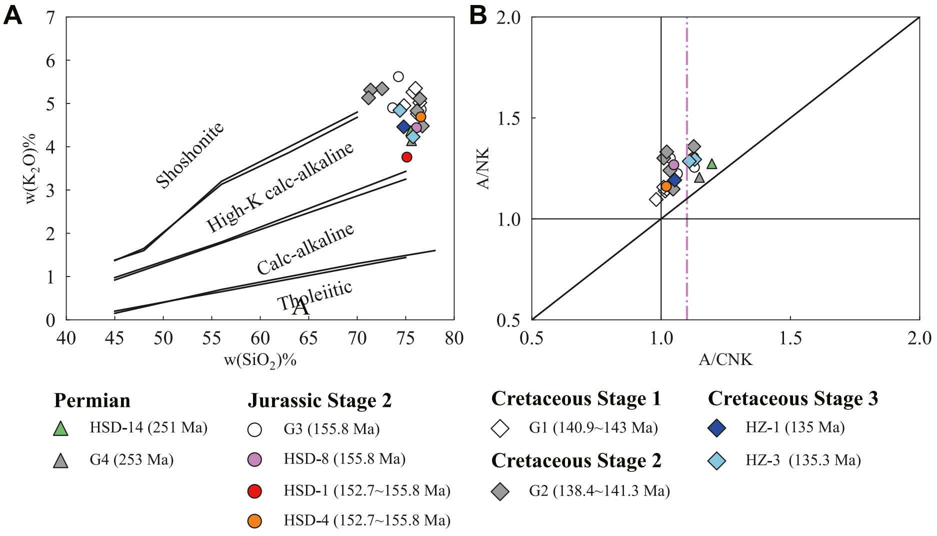

FIGURE 8
Plots of SiO_2 *versus* K_2O **(A)** and A/CNK *versus* A/NK **(B)**.

Figure 4 shows the microscopic photographs of the samples. Samples HSD-1 and HSD-8 were medium-to coarse-grained equigranular biotite granites, which contained quartz (~37 vol.%), plagioclase (~30 vol.%), alkali feldspar (~23 vol.%), biotite/muscovite (~2 vol.%), and accessory minerals (<3 vol.%), including zircon and apatite. Sample HSD-4 exhibited similar petrological features with samples HSD-1 and HSD-8, except for smaller grain sizes (fine-grained: 0.1–0.3 mm). Samples HZ-1 and HZ-3 were medium-to fine-grained equigranular biotite granites, which contained quartz (~42 vol.%), plagioclase (~29 vol.%), alkali feldspar (~23 vol.%), biotite (~2 vol.%), and muscovite (~1 vol.%). Furthermore, zircon is a common accessory mineral in these samples. In contrast, sample HSD-14 was medium-grained two-mica granite, which consisted of quartz (~40 vol.%), plagioclase (~30 vol.%), alkali feldspar (~21 vol.%), biotite (~2 vol.%), and muscovite (~2 vol.%).

4 Methods

4.1 LA-ICP-MS U-Pb dating and Hf isotopes of zircon

This study conducted zircon dating of granite samples HSD-1, HSD-4, HSD-8, HSD-14, HZ-1, and HZ-3. These six samples (~5 kg each) were processed at the Hebei Institute of Regional Geology and Mineral Resources Survey.

Six zircon grains were separated from these samples using conventional heavy-liquid and magnetic separation techniques. Then, about 100 zircon grains with the highest quality were hand-picked under a binocular microscope. These grains were mounted in epoxy and then polished. Afterward, the grains were photographed using optical microscopy and cathodoluminescence (CL) imaging to reveal their internal morphologies, which were used to select grains and analytical spots. CL images were obtained using a HITACHI S3000-N scanning electron microscope equipped with a Robinson backscattered electron detector and a Gatan Chroma CL imaging system.

To determine zircon U-Pb ages, these above samples were analyzed using an Agilent 7,900 quadrupole ICP-MS equipped with a 193 nm coherent Ar-F laser and a Resonetics S155 ablation cell at the Tianjin Institute of Geology and Mineral Resources. NIST SRM 610 glass used for Pb correction was analyzed after every 15 test samples. The mass bias of Th/U and Pb/Th ratios caused by downhole fractionation and instrumental drift was corrected using zircon reference material 91,500 following instructions of Wiedenbeck et al. (1995). Each zircon analysis involved 15 s blank gas measurement and 50 s analysis. The analytical spots were 29 μm each in size, and laser was emitted at a frequency of 7 Hz, yielding an energy density of approximately 3 J/cm^2. The grains ablated by laser were carried by He gas into the chamber at a flow rate of 0.35 L/min, where they were mixed with argon gas before being transported to the plasma torch. Zircon standards Temora (Black et al., 2003) and Plesovice (Sláma et al., 2008) were employed in this study. Data processing was performed using Concordia intercept ages on the Tera-Wasserburg plot which was prepared using ISOPLOT (Ludwig, v. 3.75, 2012). Data reduction was conducted using ICPMSDataCal (Liu et al., 2010). The random and systematic uncertainties were estimated using the method proposed by Paton et al. (2010).

Based on LA-ICP-MS zircon U-Pb dating, the cathodoluminescence (CL) diagram of zircon was plotted. The laser denudation was conducted under a beam spot diameter of 40 μm and a duration of 30 s, with GJ-1 used as the external reference material for the calculation of Hf (Geng et al., 2011). In the solution injection mode, a 200×10^{-9} standard solution was used. It was fed into a nebulizer at a flow rate of 50 μL/min using a peristaltic pump. Nine Faraday cups simultaneously received ^{172}Yb, ^{173}Yb, ^{175}Lu, ^{176}(Yb+Hf+Lu), ^{177}Hf, ^{178}Hf, ^{179}Hf, ^{180}Hf, and ^{182}W. Data acquisition was performed using the virtual amplifier technology of NEPTUNE (MC-ICPMS). The software automatically replaced

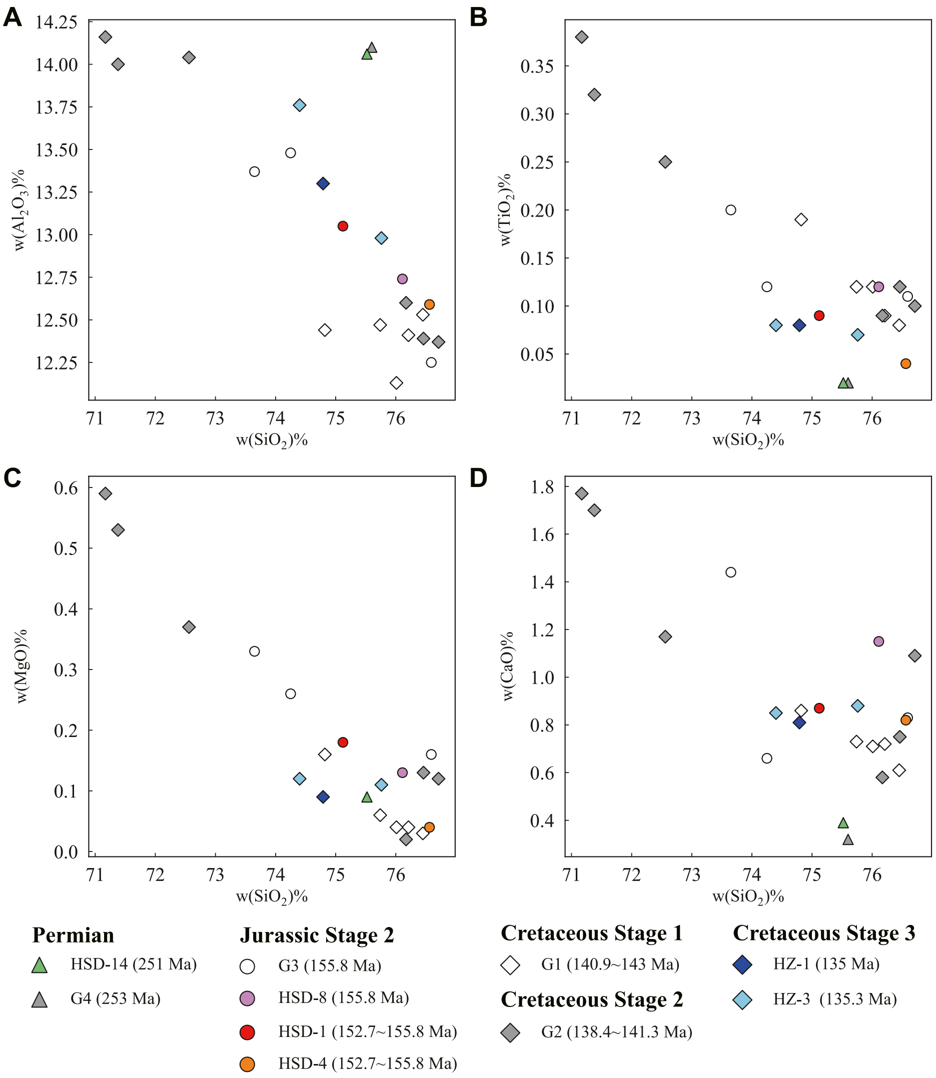

FIGURE 9
Harker diagram of the granites in the Huangshadong geothermal field **(A)** SiO_2 vs. Al_2O_3; **(B)** SiO_2 vs. TiO_2; **(C)** SiO_2 vs. MgO; **(D)** SiO_2 vs. CaO.

the amplifier circuits of the analyzer after the acquisition of a set of data. After nine sets of data were acquired, the amplifier circuits were identical to those of the original analyzer. This technique can be used to effectively eliminate the isotope ratio error caused by the difference in the gain of each Faraday cup receiver, thus improving the accuracy of isotope ratio determination.

The laser ablation test began with the targeting, polishing, and photographing of the staghornite to be tested. Samples were arranged on the double-sided adhesive of the slide and put on the PVC ring. Then, epoxy resin and hardener were mixed thoroughly and injected into the PVC ring. After the resin was fully cured, sample holders were peeled off from the slide and then polished, followed by the taking of the cathodoluminescence, reflected light, and transmitted light photographs of the samples on the target. Based on these three kinds of photographs, the appropriate area of the struvite was selected, and the struvite was stripped using a 193 nm FX laser with a spot diameter of 35, 50, or 75 (um), an energy density of 10–11 J/cm^2, and a frequency of 8–10 Hz. The laser-stripped materials were fed into the Neptune (MC-ICPMS) with high-purity He as the carrier gas. The receiver configuration was the same as that of the solution injection.

4.2 Whole-rock geochemical analyses

Seven fresh samples were cut into blocks, each measuring ~70×50×30 mm in size. These blocks were washed with tap water and ground to <200 meshes using an agate mill. Both major and trace element analyses were performed using the method proposed by Liu et al. (2016) at the Central Laboratory of China Railway Resources Group. The contents of major elements were measured using an X-ray fluorescence (XRF) spectrometer (Thermo Fisher ARL Advant'X), with the loss on ignition (LOI) being determined with an electronic analytical balance (CPA225D). The FeO content in the samples was measured using conventional

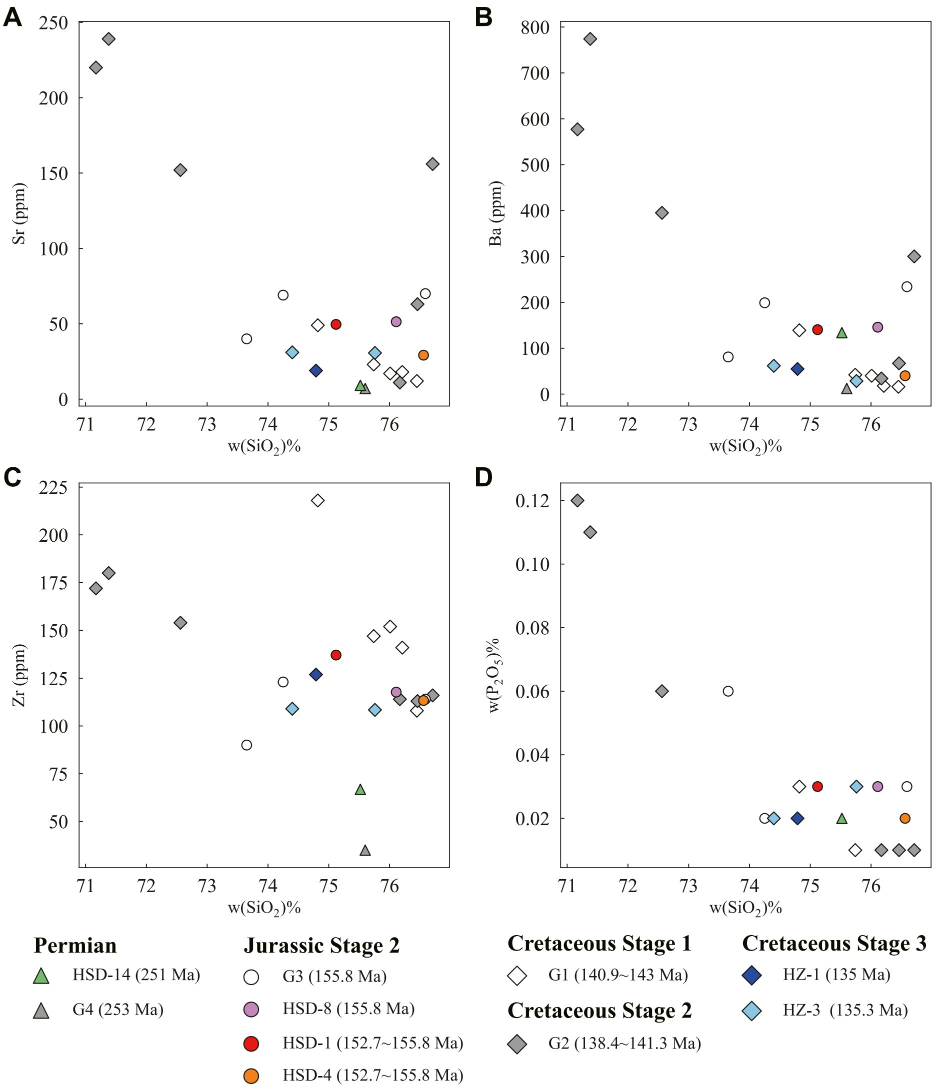

FIGURE 10
SiO_2 vs. Sr **(A)**, Ba **(B)**, Zr **(C)**, P_2O_5 **(D)** for the granites in the Huangshadong geothermal field.

wet chemical titration. The contents of trace elements, including rare earth elements (REEs), were determined using ICP-MS (Thermo Fisher X-series 2) after complete digestion. A detailed account of the test procedures and the lower detection limit were documented in Chinese national standard GB/T14506-2010 (Lv, 2010). The analytical errors varied in a range of 1%–3% of the present values. The whole-rock geochemical analyses were conducted under temperatures of 20–27°C and humidity of 30%–58%.

5 Results

5.1 Zircon dating

As presented in Figure 5, zircons from sample HZ-1 were typically transparent, ranging from colorless to slightly brown, and exhibited rectangular to prismatic crystal structures. They were 80–180 μm long, with aspect ratios ranging from 1.5:1 to 3:1. Furthermore, these crystals commonly exhibited oscillatory zoning (Figure 5). Zircons from sample HZ-3 were predominantly transparent, clear to pale yellow, and euhedral to subhedral crystals. They were 70–170 μm long, with aspect ratios varying in the range of 2:1–3:1. Among them, euhedral grains showed concentric zoning with relatively bright cores, as shown in CL images (Figure 5). Zircons from samples HSD-1 and HSD-8 were similar in shape and color. They were slightly larger (typical length: 100–200 μm), with aspect ratios between 1:1 and 3:1, and exhibited weakly oscillatory zoning. Furthermore, zircons from sample HSD-4 were considerably smaller (length: 40–100 μm), with aspect ratios of 1:1–4:1.

The LA-ICP-MS zircon U-Pb ages of the HGF are shown in Figure 6; Table 2. Fifteen analyses showed that sample HZ-1 had a^{238}U/^{206}Pb age of 135 ± 4 Ma (MSWD = 5.7), while 20 analyses revealed that sample HZ-3 had a weighted average ^{238}U/^{206}Pb age of 135.3 ± 2.4 Ma (MSWD = 3.2). The two ages, which were consistent

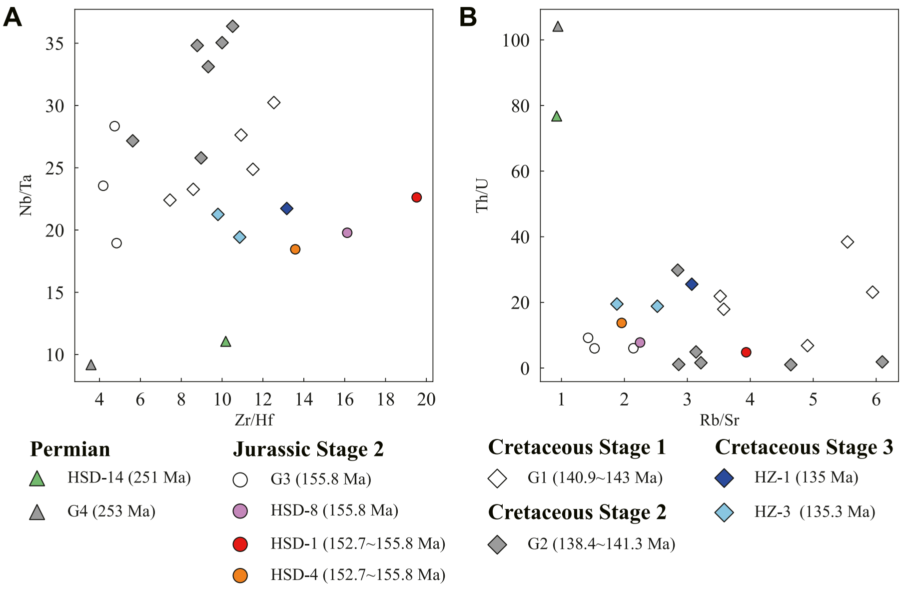

FIGURE 11
Zr/Hf vs Nb/Ta **(A)**, Rb/Sr vs Th/U **(B)** for the granites in the Huangshadong geothermal field.

within the given error range, indicate that both samples formed during the Cretaceous. In contrast, samples HSD-1, HSD-4, and HSD-8 exhibited significantly older weighted average ^{238}U/^{206}Pb ages of 152.7 ± 2.7 Ma (MSWD = 4.8), 155.8 ± 3.3 Ma (MSWD = 5.2), and 153 ± 3 Ma (MSWD = 3.8), respectively. These ages, which were also consistent within the given error range, suggest that these three samples intruded during the Jurassic. Sample HSD-14 was emplaced during the Indosinian, as indicated by four data points yielding a^{238}U/^{206}Pb age of 153.7 ± 1.2 (MSWD = 2.2; probability = 0.002). As shown in Figure 7; Table 3, sample HSD-14 exhibited the highest Ti-in-zircon temperatures from 684°C to 781°C (Ferry and Watson, 2007), with an average of 742°C, while the other samples had lower Ti-in-zircon temperatures, with averages ranging from 617°C to 687°C.

5.2 Geochemical characteristics

We analyzed the major and trace element compositions of seven representative samples (Table 5). These samples featured high SiO_2 (74.4–76.56 wt.%) and K_2O (3.76–4.84 wt.%) contents. All the samples fell within the high-K calc-alkaline zone (Figure 8A). Samples HSD-4, HSD-8, and HZ-1 exhibited aluminum saturation index (ASI) values of 1.02, 1.05, and 1.05, respectively, all of which were less than 1.1 (Figure 8B). In comparison, samples HSD-1, HZ-3-1, and HZ-3-2 had ASI values of 1.13, 1.13, and 1.11, respectively, all of which were greater than 1.1.

Compared to the other samples, samples HSD-1, HSD-8, and HSD-14 had higher K_2O, CaO, MgO, TiO_2, Zr, Sr, and Ba contents but lower Na_2O and Al_2O_3 contents (Figures 8–11; Table 5). All these samples were depleted in P_2O_5 (Figure 11).

As shown in the primitive mantle-normalized diagrams (Figure 12; Table 5), sample HSD-14 exhibited the strongest depletion in Ti, Sr, La, and Ce but notable enrichment in Rb, U, and Nd. Compared with samples HSD-1 and HSD-8, samples HSD-4, HZ-1, and HZ-3 were relatively depleted in Ti, Sr, and Ba but enriched in Rb, U, Nb, and Nd.

The REE patterns (Figure 13; Table 5) showed that sample HSD-14 exhibited a leftward REE pattern with the lowest La_N/Yb_N ratio (0.56); samples HZ-3-1 and HZ-3-2 showed relatively flat patterns with similar La_N/Yb_N ratios of 1.47 and 1.32, respectively; sample HZ-1 had a much higher La_N/Yb_N ratio of 9.7; among the remaining samples, HSD-1 displayed the highest La_N/Yb_N ratio (5.06), followed by HSD-8 (2.95), while HSD-4 had the lowest La_N/Yb_N ratio (1.19); samples HSD-4, HSD-14, HZ-3-1, and HZ-3-2 exhibited the lowest δEu values, which were 0.1, 0.1, 0.09, and 0.07, respectively, while sample HSD-1 had the highest δEu value, which was 0.32. The Indosinian granite (sample HSD-14) exhibited relatively low total REE contents (ΣREE; 78.38). In contrast, the Cretaceous granites showed the highest ΣREEs, with values of 188.55 ppm, 111.12 ppm, and 149.78 ppm for samples HZ-1, HZ-2, and HZ-3, respectively.

5.3 Hf isotopes

This study conducted the Lu-Hf isotope analyses for zircons that were subjected to U-Pb dating, as shown in Table 6; Figure 14. Specifically, Lu-Hf isotope analysis was conducted on 15 and 20 zircon grains from HZ-1 and HZ-3, respectively. These zircons show a wide range of^{176}Yb/^{177}Hf ratios from 0.017479 to 0.126740 (average: 0.050829) and ^{176}Lu/^{177}Hf ratios between 0.000509 and 0.003495 (average: 0.00132), indicating low content of radiogenic Hf. Furthermore, 35 analytical spots yielded $\varepsilon_{Hf}(t)$ values of −11.4334 to −3.0396, which corresponded to two-stage Hf model ages (T_{DM2}) of 1,385–1907 Ma dominated by 1,500–1700 Ma, as depicted in Figure 15.

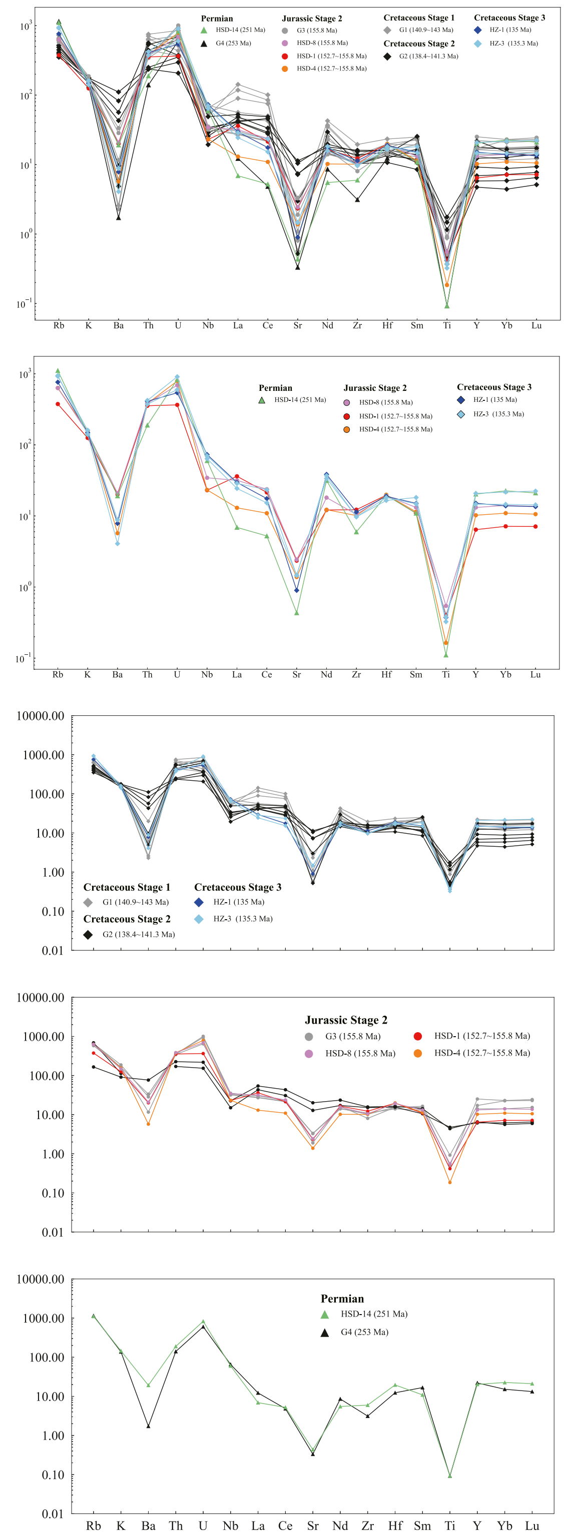

FIGURE 12
Primitive mantle-normalized trace element spider diagrams of granites in the Huangshadong geothermal field (Sun and McDonough, 1989).

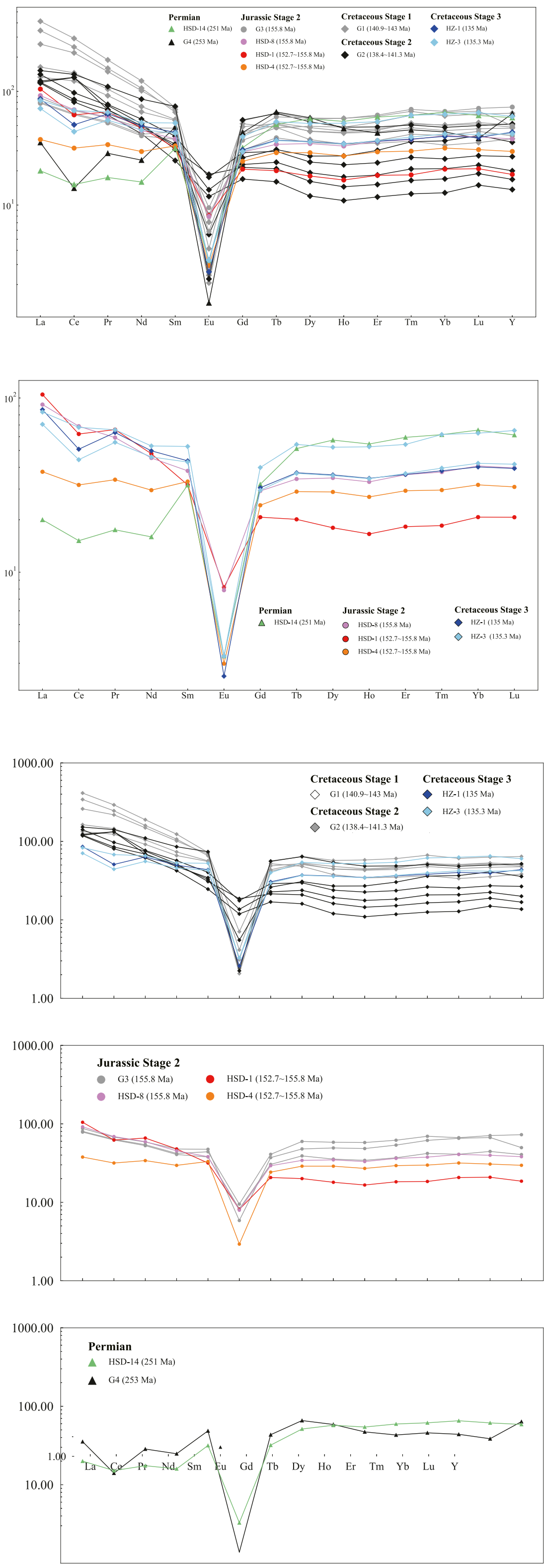

FIGURE 13
Chondrite-normalized REE spider diagrams of granites in the Huangshadong geothermal field (Sun and McDonough, 1989).

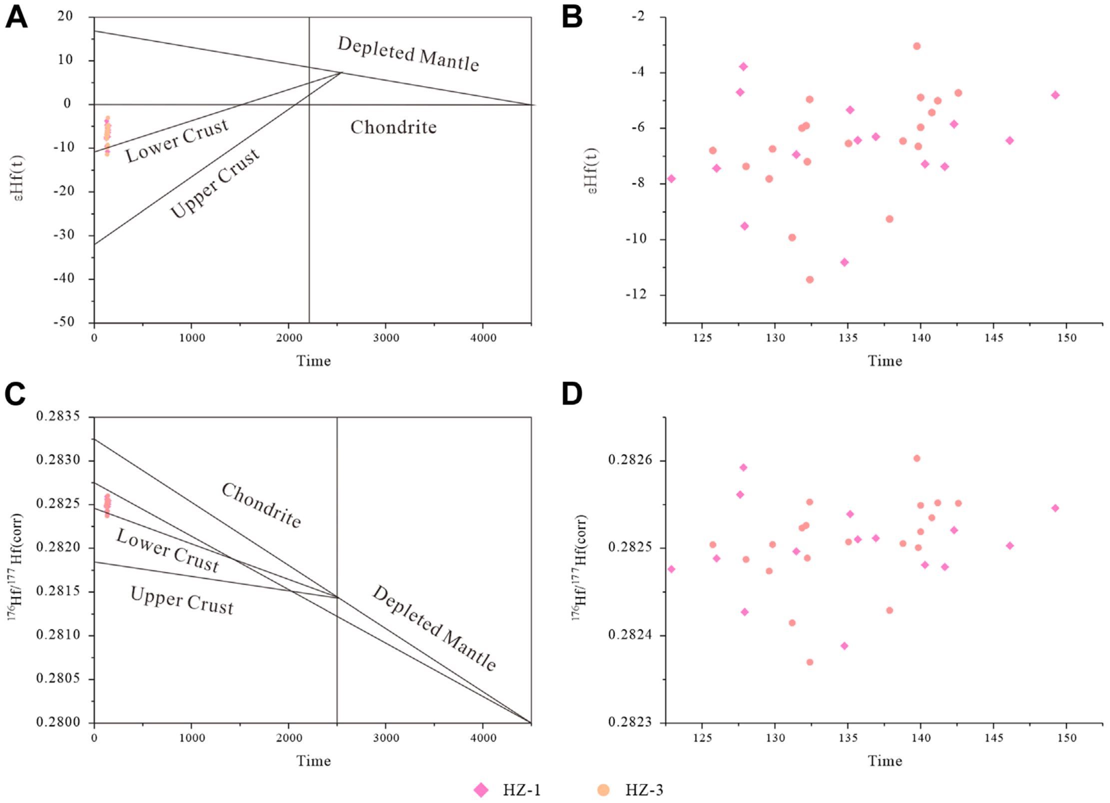

FIGURE 14
Zircon Lu-Hf isotopic compositions for the Cretaceous granite in (geothermal reservoir rock) the Huangshadong geothermal field.

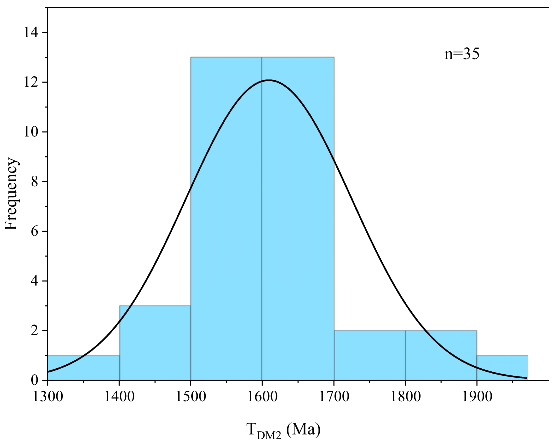

FIGURE 15
Histogram of T_{DM2} for the Cretaceous granite complex.

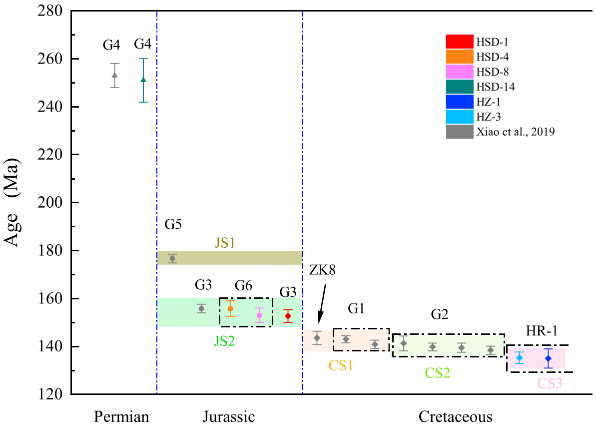

FIGURE 16
Zircon ages of granites in the Huangshadong geothermal field (Xiao et al., 2019). JS1: Jurassic stage 1; JS1: Jurassic stage 2; CS1: Cretaceous stage 1; CS2: Cretaceous stage 2; CS3: Cretaceous stage 3.

6 Discussion

6.1 Timing of granite emplacement

The zircon ages of the granites in the HGF are summarized in Table 4; Figure 16. These ages indicate three stages of granite emplacement: 1) the Indosinian stage, corresponding to Permian granites (251 ± 9.1 to 253 ± 5 Ma); 2) the Yanshanian stage, including Jurassic granites (152.7 ± 2.7–176.7 ± 1.8 Ma); 3) the Cretaceous stage (135 ± 4–143.6 ± 2.8 Ma) (Xiao et al., 2019). These ages indicate intense

TABLE 4 Zircon ages of the igneous rocks in the Huangshadong geothermal field.

Era	Sample	Age (Ma)	Age error (Ma)	Source	Group	HP
Permian	Id-30	253	5	Xiao et al. (2019)	G4	4.26
Permian	HSD-14	251	9.1	This study		6.14
Jurassic	Is-02	176.7	1.8	Xiao et al. (2019)	G5	2.62
Jurassic	Id-04	155.8	1.8	Xiao et al. (2019)	G3	5.76
Jurassic	HSD-1	152.7	2.7	This study		4.51
Jurassic	HSD-4	155.8	3.3	This study		7.12
Jurassic	HSD-8	153	3	This study		6.56
Cretaceous	Id-33	143.6	2.8	Xiao et al. (2019)	ZK8	3.16
Cretaceous	Id-24	143	1.5	Xiao et al. (2019)	G1	6.35
Cretaceous	Id-22	140.9	1.7	Xiao et al. (2019)	G1	4.83
Cretaceous	Id-10	141.3	3.1	Xiao et al. (2019)	G2	6.17
Cretaceous	Id-11	139.8	1.6	Xiao et al. (2019)	G2	3.69
Cretaceous	Id-08	139.5	1.9	Xiao et al. (2019)	G2	3.23
Cretaceous	Id-12	138.4	1.7	Xiao et al. (2019)	G2	2.83
Cretaceous	HZ-3	135.3	2.4	This study	HR-1	7
Cretaceous	HZ-1	135	4	This study	HR-1	5.88

Note: HP, denotes heat production (unit: mW/m^3).

Mesozoic (Yanshanian) magmatic activity in the study area. The Cretaceous granites dominate the HGF, exhibiting the largest outcrop area (100 km^2; Figure 2), while the Permian granites only occur in the northern part of the geothermal field (Xiao et al., 2019). As indicated by the zircon dating results of samples HZ-1 and HZ-3 taken from the deep part of well HR-1, the surrounding rocks of the geothermal reservoirs in the HGF consist of Cretaceous granites, although Permian granites are the closest to geothermal wells (HR-1 and ZK8).

6.2 Petrogenesis of granites

As shown in the Harker diagram, the samples collected in this study were the product of felsic magmas and had undergone significant fractionation. The Yanshanian granites, represented by the samples collected in this study, show a downward trend of Al, Mg, and Ca contents with an increase in the SiO_2 content (degree of fractionation; Figure 9). The depletion in Sr, Ba, and Ti, as well as prominent negative Eu anomalies (Figure 10), is indicative of the fractionation of plagioclase and Ti-Fe oxides. Figure 11 illustrates decreases in the Zr/Hf, Nb/Ta, and Th/U ratios but increases in the Rb/Sr ratio with an increase in the degree of magmatic fractionation (Stepanov et al., 2016; Breiter and Škoda, 2017; Cai et al., 2020). Furthermore, samples collected from or around geothermal wells exhibited significantly V-shaped REE patterns than those collected at a greater distance from geothermal wells, indicating that they underwent a higher degree of crystal fractionation.

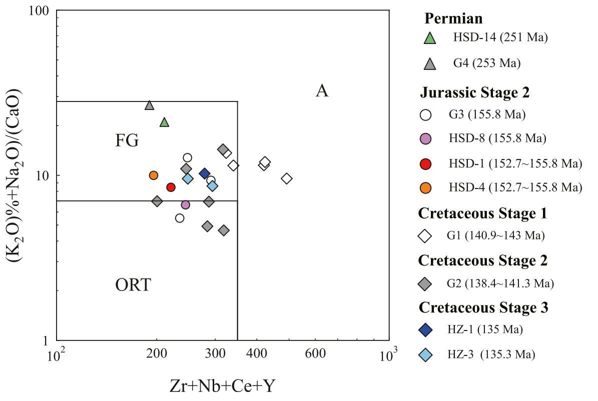

FIGURE 17
Discriminant diagrams of the granites in the Huangshadong geothermal field (Whalen et al., 1987). FG denotes fractionated felsic granites; OGT denotes unfractionated M-, I- and S-type granites.

TABLE 5 Geochemical contents of the igneous rocks in the Huangshadong geothermal field.

Element	HSD-1	HSD-4	HSD-8	HSD-14	HZ-1	HZ-3–1	HZ-3–2
SiO_2 (%)	75.12	76.56	76.11	75.52	74.79	74.4	75.76
Al_2O_3	13.05	12.59	12.74	14.06	13.3	13.76	12.98
Fe_2O_3	1.45	1.07	1.47	0.66	1.25	1.21	1.26
MgO	0.18	0.04	0.13	0.09	0.09	0.12	0.11
CaO	0.87	0.82	1.15	0.39	0.81	0.85	0.88
Na_2O	3.6	3.5	3.18	3.83	3.84	3.27	3.35
K_2O	3.76	4.69	4.44	4.37	4.46	4.84	4.23
MnO	0.03	0.05	0.05	0.09	0.03	0.06	0.06
TiO_2	0.09	0.04	0.12	0.02	0.08	0.08	0.07
P_2O_5	0.03	0.02	0.03	0.02	0.02	0.02	0.03
LOI	1.78	0.59	0.53	0.92	1.3	1.36	1.25
FeO	1.05	0.94	1.05	0.25	1.03	0.8	0.75
K_2O+Na_2O	7.36	8.19	7.62	8.2	8.3	8.11	7.58
Li (ppm)	11.78	15.39	106.5	19.16	17.01	12.97	12.26
Be	3.92	7.46	5.96	9.08	4.9	4.83	5.05
Sc	2.28	1.82	3.28	4.94	4.08	3.58	4.51
V	0.91	0.15	7.28	0.84	2.29	5.94	2.69
Cr	3.9	4.62	4.12	3.1	4.4	4.83	1.98
Co	0.57	0.29	1.01	0.66	0.83	0.6	0.47
Ni	1.49	1.52	1.73	1.78	1.36	1.24	4
Cu	1.61	1.2	1.75	3.78	2.64	2.75	0.87
Zn	7.87	10.96	26.4	34.41	16.93	24.15	19.68
Ga	16.81	18.27	17.63	24.35	19.6	22.88	20.58
Rb	238.1	400.8	399.6	703.3	483.7	584.3	597.9
Sr	49.59	29.17	51.35	9.16	18.94	31.03	30.65
Zr	137.1	113.3	117.7	66.82	126.9	109	108.4
Nb	16.4	16.57	24.51	42.65	52.01	45.51	49.87
Cs	3.28	7.28	14.73	37.65	5.11	9.78	8.55
Ba	140.4	39.94	145.8	133.8	54.77	61.62	28.49
Mo	0.46	0.32	0.82	0.24	0.99	0.72	0.46
In	0.02	0.02	0.06	0.13	0.04	0.07	0.06
Hf	6.06	6.14	5.95	6.04	5.84	5.61	5.1
Ta	0.84	1.22	1.52	4.19	3.95	4.19	5.09

(Continued on the following page)

TABLE 5 (*Continued*) Geochemical contents of the igneous rocks in the Huangshadong geothermal field.

Element	HSD-1	HSD-4	HSD-8	HSD-14	HZ-1	HZ-3–1	HZ-3–2
W	3.98	1.78	6.48	2.65	3.47	1.27	2.36
Tl	1.16	1.94	1.91	4.34	1.8	1.99	1.93
Pb	20.13	39.93	44.26	198.1	22.25	37.75	36.74
Bi	0.39	3.79	1.54	9.7	0.09	0.64	0.54
Th	30.14	32.44	32.61	16.07	34.82	31.72	35.83
U	7.66	16.58	14.5	17.39	11.34	12.57	19.05
Y	29.19	46.51	59.83	92.17	68.7	66.51	94.48
La	24.81	8.94	21.73	4.74	20.32	16.74	19.69
Ce	38.03	19.39	42.15	9.28	31.1	27.07	41.52
Pr	6.26	3.23	5.63	1.66	6.02	5.29	6.24
Nd	22.34	13.81	21.13	7.45	23.23	21.42	24.78
Sm	4.85	5.07	5.84	4.84	6.67	6.56	8.06
Eu	0.47	0.17	0.46	0.19	0.15	0.19	0.19
Gd	4.25	4.98	6.01	6.57	6.28	6.07	8.2
Tb	0.75	1.08	1.28	1.92	1.39	1.38	2.02
Dy	4.57	7.33	8.82	14.56	9.19	9.12	13.25
Ho	0.94	1.53	1.87	3.08	1.96	1.95	2.97
Er	3.02	4.86	6	9.84	6.03	6.09	8.96
Tm	0.47	0.76	0.96	1.57	0.97	1.01	1.57
Yb	3.52	5.39	6.93	11.12	6.83	7.17	10.68
Lu	0.53	0.78	1.01	1.56	1	1.06	1.65
Y+Nb	45.59	63.08	84.34	134.82	120.71	112.02	144.35
ΣREE	114.81	77.32	129.82	78.38	188.55	111.12	149.78
LREE	96.76	50.61	96.94	28.16	170.93	77.27	100.48
HREE	18.05	26.71	32.88	50.22	17.62	33.85	49.3
LREE/HREE	5.36	1.89	2.95	0.56	9.7	2.28	2.04
La_N/Yb_N	5.06	1.19	2.25	0.31	12.44	1.67	1.32
δEu	0.32	0.1	0.24	0.1	0.16	0.09	0.07
δCe	0.75	0.88	0.93	0.81	0.81	0.71	0.92
10000Ga/Al	2.43	2.74	2.61	3.27	2.78	3.14	2.99
Zr+Nb+Ce+Y	220.72	195.77	244.19	210.92	278.71	248.09	294.27
$(K_2O+Na_2O)/CaO$	8.43	9.98	6.6	21.23	10.23	9.49	8.65
Rb/Sr	4.8	13.7	7.8	76.8	25.5	18.8	19.5

(Continued on the following page)

TABLE 5 (*Continued*) Geochemical contents of the igneous rocks in the Huangshadong geothermal field.

Element	HSD-1	HSD-4	HSD-8	HSD-14	HZ-1	HZ-3–1	HZ-3–2
A/CNK	1.13	1.02	1.05	1.20	1.05	1.13	1.11
A/NK	1.30	1.16	1.27	1.27	1.19	1.29	1.28
Th/U	3.94	1.96	2.25	0.92	3.07	2.52	1.88
Heat production	4.51	7.12	6.56	6.14	5.88	6.02	7.99

Note: $T_{Ti\text{-}zircon}$ indicates the saturation temperature of Ti in zircon. La_N/Yb_N denotes the ratio of La to Yb contents normalized to chondrite. A/CNK, denotes molar ratio of $Al_2O_3/(CaO + Na_2O + K_2O)$; A/NK, denotes molar ratio of $Al_2O_3/(Na_2O + K_2O)$. The unit of Heat production is $\mu W/m^3$.

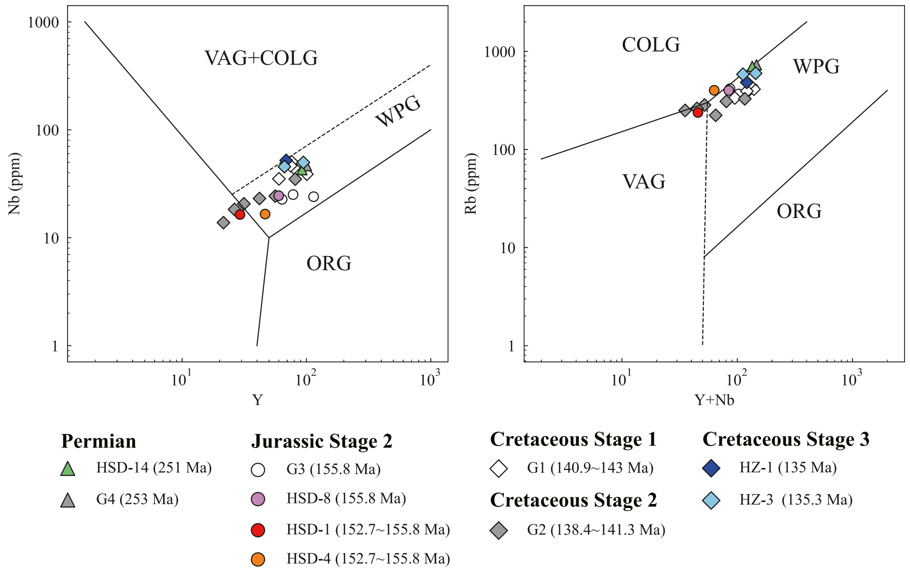

FIGURE 18
Tectonic setting discrimination diagrams of the granites in the Huangshadong geothermal field (after Pearce et al. (1984)). VAG. Volcanic-arc granite; syn-COLG. syn-collisional granite, WPG: within-plate granite; ORG: ocean-ridge granite.

Generally, granites can be categorized into S-, I-, A-, and M-types based on their genesis (Collins et al., 1982; Chappell and White, 2001; Chappell et al., 2012; Zhou et al., 2021). S-type granites originate from sedimentary rocks (Chappell et al., 1999), while I-type granites originate from ancient igneous rocks (Chappell and White, 2001). A-type granites are generally formed by the partial melting of dry granulitic residues in the lower crust, featuring a high abundance of large highly charged cations (Nb, Ga, and REEs) and low Mg, Ca, and Al content (Collins et al., 1982). M-type granites are derived from the subducted oceanic crust or overlying mantle (Whalen et al., 1987). A/CNK serves as an effective factor used to distinguish between S- and I-type granites (Chappell and White, 2001). Sample HSD-14 (Permian granites) had an A/CNK value of 1.2, suggesting that it was S-type granite. This result is consistent with the presence of primary muscovite (Figure 4). In contrast, Yanshanian granites (Jurassic and Cretaceous stages) exhibit A/CNK values of 1.05–1.13, ruling out the possibility of them being S-type granites. As presented in Figure 17, these Yanshanian granites fall within the zone of fractionated granites, suggesting that these granites are highly fractionated I-type granites rather than A-type granites. This finding is consistent with the downward trend of P content with an increase in the SiO_2 content (Figure 10) and can also be evidenced by low Ti-in-zircon temperatures of 475–781°C (Table 3; Figure 7).

Zircon Lu-Hf isotope compositions are an important tool for identifying the magma source of granites (Bhattacharya and Janwari, 2015; Bea et al., 2018). As indicated by the Hf isotope composition and T_{DM2} ages (1,385–1907 Ma) of samples HZ-1 and HZ-3, collected at depths of 2,637 m and 2,702 m, respectively (Table 6; Figures 14, 15), the reservoir granites originated from the mixing of Meso-to Paleo-Proterozoic lower crust and juvenile mantle materials. Two theories have been proposed for the formation of highly fractionated I-type granites, namely, the partial melting of crustal materials (Chappell et al., 1999; Wyborn et al., 2001) and the fractional crystallization of mafic melts (Chappell et al., 1999; Chappell et al., 2012). The latter assumption can be excluded for the following reasons: 1) such a large volume of granitoids (80%) is difficult to form due to the too small quantity of mafic

TABLE 6 Hf isotopic data of zircon grains for the granites (HZ-1 and HZ-3) in the Huangshadong geothermal field.

Spot	Age (Ma)	$^{176}Hf/^{177}Hf$	2σ	$^{176}Yb/^{177}Hf$	2σ	$^{176}Lu/^{177}Hf$	2σ	$\varepsilon_{Hf}(0)$	$\varepsilon_{Hf}(t)$	T_{DM1} (Ma)	T_{DM2} (Ma)	fLu/Hf
Sample HZ-1												
HZ-1–1	149	0.282546	0.000029	0.031113	0.000494	0.000838	0.000007	−8.0	−4.8	994	1,503	−0.97
HZ-1–2	137	0.282512	0.000013	0.033321	0.000519	0.001061	0.000015	−9.2	−6.3	1,049	1,589	−0.97
HZ-1–3	126	0.282488	0.000024	0.092604	0.002119	0.002087	0.000042	−10.0	−7.4	1,112	1,652	−0.94
HZ-1–4	142	0.282479	0.000022	0.047657	0.000391	0.001233	0.000005	−10.4	−7.4	1,100	1,660	−0.96
HZ-1–5	128	0.282593	0.000025	0.116845	0.002550	0.002742	0.000049	−6.3	−3.8	979	1,422	−0.92
HZ-1–6	131	0.282496	0.000018	0.035996	0.000882	0.000948	0.000018	−9.7	−6.9	1,067	1,625	−0.97
HZ-1–7	128	0.282562	0.000024	0.027990	0.001074	0.000714	0.000015	−7.4	−4.7	970	1,480	−0.98
HZ-1–8	135	0.282539	0.000021	0.028621	0.000077	0.000821	0.000004	−8.2	−5.3	1,004	1,526	−0.98
HZ-1–9	136	0.282510	0.000020	0.059804	0.000345	0.001659	0.000008	−9.3	−6.4	1,068	1,596	−0.95
HZ-1–10	135	0.282388	0.000025	0.113988	0.003221	0.002252	0.000078	−13.6	−10.8	1,262	1870	−0.93
HZ-1–11	128	0.282427	0.000024	0.054964	0.001335	0.001474	0.000028	−12.2	−9.5	1,180	1783	−0.96
HZ-1–12	142	0.282521	0.000021	0.037839	0.000765	0.000987	0.000011	−8.9	−5.9	1,034	1,564	−0.97
HZ-1–13	140	0.282481	0.000020	0.027054	0.000059	0.000763	0.000004	−10.3	−7.3	1,083	1,653	−0.98
HZ-1–14	123	0.282476	0.000022	0.017479	0.000097	0.000509	0.000001	−10.5	−7.8	1,083	1,672	−0.98
HZ-1–15	146	0.282503	0.000020	0.049758	0.000320	0.001322	0.000010	−9.5	−6.4	1,068	1,604	−0.96
Sample HZ-3												
HZ-3–1	126	0.282504	0.000021	0.034011	0.000318	0.000937	0.000013	−9.5	−6.8	1,056	1,611	−0.97
HZ-3–2	140	0.282549	0.000019	0.029258	0.000173	0.000819	0.000003	−7.9	−4.9	990	1,502	−0.98
HZ-3–3	140	0.282501	0.000019	0.051344	0.000835	0.001323	0.000012	−9.6	−6.6	1,072	1,612	−0.96
HZ-3–4	132	0.282526	0.000025	0.044628	0.001340	0.001252	0.000032	−8.7	−5.9	1,034	1,560	−0.96
HZ-3–5	140	0.282519	0.000021	0.034067	0.000131	0.000951	0.000002	−8.9	−6.0	1,035	1,570	−0.97
HZ-3–6	135	0.282507	0.000022	0.056072	0.000266	0.001536	0.000011	−9.4	−6.5	1,069	1,602	−0.95

(Continued on the following page)

TABLE 6 (*Continued*) Hf isotopic data of zircon grains for the granites (HZ-1 and HZ-3) in the Huangshadong geothermal field.

Spot	Age (Ma)	$^{176}Hf/^{177}Hf$	2σ	$^{176}Yb/^{177}Hf$	2σ	$^{176}Lu/^{177}Hf$	2σ	$\varepsilon_{Hf}(0)$	$\varepsilon_{Hf}(t)$	T_{DM1} (Ma)	T_{DM2} (Ma)	fLu/Hf
HZ-3–7	130	0.282474	0.000018	0.049061	0.000713	0.001347	0.000027	−10.5	−7.8	1,110	1,678	−0.96
HZ-3–8	131	0.282415	0.000027	0.085464	0.004156	0.001932	0.000093	−12.6	−9.9	1,213	1812	−0.94
HZ-3–9	132	0.282523	0.000019	0.034128	0.000205	0.000979	0.000010	−8.8	−6.0	1,030	1,565	−0.97
HZ-3–10	138	0.282429	0.000022	0.065247	0.001786	0.001604	0.000041	−12.1	−9.3	1,182	1775	−0.95
HZ-3–11	132	0.282370	0.000019	0.046609	0.001613	0.001235	0.000051	−14.2	−11.4	1,254	1907	−0.96
HZ-3–12	140	0.282603	0.000025	0.055780	0.001370	0.001417	0.000025	−6.0	−3.0	929	1,385	−0.96
HZ-3–13	132	0.282553	0.000027	0.046366	0.000402	0.001290	0.000015	−7.7	−5.0	997	1,500	−0.96
HZ-3–14	141	0.282552	0.000018	0.126740	0.001240	0.003495	0.000018	−7.8	−5.0	1,060	1,510	−0.89
HZ-3–15	141	0.282535	0.000017	0.055659	0.000292	0.001494	0.000009	−8.4	−5.4	1,028	1,537	−0.95
HZ-3–16	139	0.282506	0.000021	0.031541	0.000079	0.000854	0.000005	−9.4	−6.5	1,052	1,600	−0.97
HZ-3–17	143	0.282552	0.000020	0.024341	0.000110	0.000685	0.000001	−7.8	−4.7	983	1,494	−0.98
HZ-3–18	128	0.282487	0.000019	0.044336	0.000170	0.001267	0.000004	−10.1	−7.4	1,089	1,649	−0.96
HZ-3–19	130	0.282504	0.000022	0.053297	0.000678	0.001428	0.000017	−9.5	−6.7	1,070	1,611	−0.96
HZ-3–20	132	0.282489	0.000017	0.036022	0.000283	0.000949	0.000002	−10.0	−7.2	1,078	1,641	−0.97

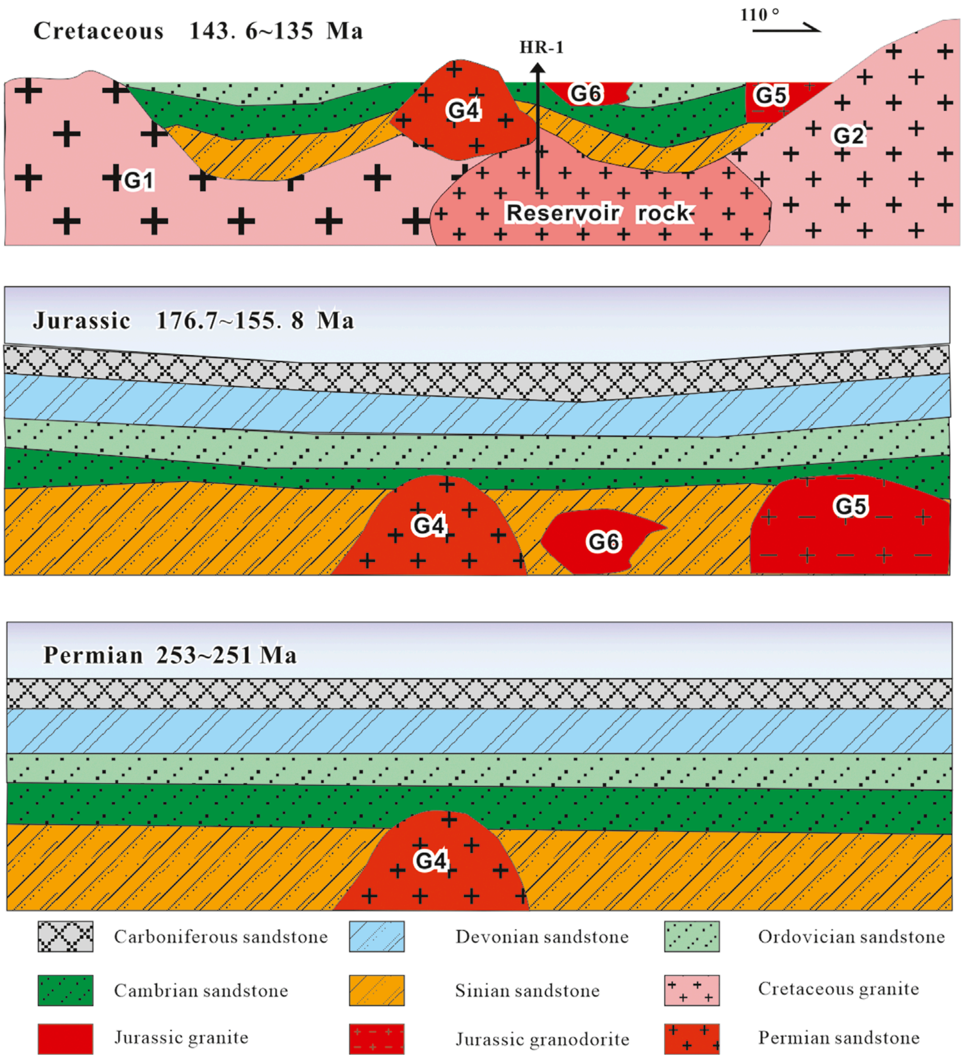

FIGURE 19
Magmatism evolution of Huangshadong geothermal field (the location of profile is shown in Figure 2).

rocks within igneous rocks (Zhang et al., 2015); 2) the parent magmas (peraluminous melts) of I-type granites are unlikely to be produced through the fractional removal of hornblende (Chappell et al., 2012). Instead, Cretaceous I-type granites in the study area are likely derived from the partial melting of the lower crust. Since the Early Jurassic (~190 Ma), the Cathaysia Block had experienced asthenospheric upwelling and intra-continental lithosphere extension after the Indosinian flat-slab subduction of the Paleo-Pacific plate (Li and Li, 2007; Chen et al., 2008). As presented in Figure 18, these granites fall within the plate granite (WPG) zone, indicating an extensional setting. This finding is consistent with the Jurassic-Cretaceous coastward migration of extensional magmatism in the South China Block (Li and Li, 2007; Qiu et al., 2017), during which mafic magmas produced by the partial melting of the asthenospheric mantle triggered the partial melting of lower crust materials and the following generation of felsic magmas. This conclusion accords with the presence of gabbro-basalt rocks (height: 5 km) in the middle crust (depth: 20 km) (Zhang et al., 2005; Zhang et al., 2013).

6.3 Contributions of cretaceous granites to geothermal resources

Granites that have heat production rates >5 $\mu W/m^3$ are classified as high-heat-producing granites, which have significant effects on the surface heat flow. The presence of high-heat-producing granites at depths of 1,650–2,980 m can increase the surface heat flow from the background value of 68 mW/m^2 to 93 mW/m^2, with an increase by 40% (Wang et al., 2023). Compared to magmas, radioactive heat causes a much lower increase in temperature but an extremely longer timespan of thermal anomalies. Mclaren et al. (1999) attributed the temperature increase of 40°C in the contact zone between plutons and host rocks to the decay of radiogenic elements. In the HGF, the Yanshanian granites exhibit heat production rates of 4.51–7.99 $\mu W/m^3$, averaging 6.35 $\mu W/m^3$ (Table 5). Therefore, they are high-heat-producing granites. Furthermore, the Cretaceous and Jurassic granites have average heat production rates of 6.63 $\mu W/m^3$ and 6.06 $\mu W/m^3$, respectively (Table 5).

According to lithological records and zircon ages (Tables 2, 6; Figures 6, 16), the concealed Cretaceous granites in the HGF occur at depths of 1,560–3,000 m in geothermal well HR-1 (Li et al., 2020b). The large volume of high-heat-producing Cretaceous granites (geothermal reservoir rocks) is an important heat source of geothermal resources in the study area. The surface heat flow of the HGF is 115.5 mW/m^2, about 1.6 times the background heat flow (73 mW/m^2) (Xi et al., 2021). In sum, the heat production of Cretaceous granites plays a major role in the formation of geothermal resources in the HGF.

6.4 Magmatism evolution model

Previous studies summarized the regional petrogeological characteristics of granites based on granite samples collected from outcrops at a greater distance from HGF (G1, G2, G3, and G5 in Figure 2; Xiao et al., 2019). By comparison, all the samples used in this study were collected from or around geothermal wells (e.g., HR-1) to figure out the petrogenesis of geothermal reservoir rocks buried at depth and the magmatism evolution model of the HGF. As shown by the sampling locations and zircon ages of the samples (Figures 2, 5; Table 4), the ages of the Yanshanian granites exhibit a downward trend from the periphery to the center of the HGF (geothermal wells HR-1 and ZK8). In other words, the geothermal resources are hosted by relatively younger Yanshanian granites. Most especially, for Cretaceous granites, Xiao et al. (2019) obtained the emplacement ages ranging from 138.4 to 143.6 Ma based on the zircon dating of granite samples from G1, G2, and 300 m at the depth of ZK8 (Figure 2; Table 4). This study discovered that the reservoir granites at depth (~3,000 m) intruded later than the upper and outer Cretaceous granites, with an emplacement age of ~135 Ma. The reservoir granites exhibit the flattest REE pattern, indicating the strongest fractional crystallization among Cretaceous granites. This result accords with their higher heat generation. Their average heat production (HZ-1 and HZ-3, Table 4) is 6.44 $\mu W/m^3$, while that of the upper (Id-33, 3.16 $\mu W/m^3$) and outer (4.51 $\mu W/m^3$) granites is much lower (representative samples: G1, G2; Figures 10–13). Regarding the Jurassic granites, two zircon ages were obtained by Xiao et al. (2019): 155.8 Ma for G3 and 176.7 Ma for G5. These ages indicate two episodes of Jurassic magmatism in the HGF. The intrusion ages of the Jurassic granites (HSD-1, HSD-4) exposed around the geothermal wells are consistent with those of granites (HSD-8) collected from G3 within the error range. This suggests that the Jurassic granites around the geothermal wells should be formed during the later Jurassic magmatic event (JS 2 in Figure 16) recorded by Xiao et al. (2019). Their average heat production rate (5.99 $\mu W/m^3$, average value from HSD-1, HSD-4, HSD-8, and Id-04) is twice that (2.62 $\mu W/m^3$) of granodiorites formed during the former Jurassic magmatic event. It is noteworthy that fine-grained equigranular biotite granites (HSD-4) intruded into HSD-1 (Figure 3) exhibit the strongest depletion of Ba, Nb, Sr, and Ti (Figure 12) and significant Eu anomalies (Figure 13) in the Jurassic granites, suggesting that they have undergone the strongest fractional differentiation (Chen et al., 2014; Liao et al., 2021). This implies that these granites are the latest phase of Jurassic granites.

In sum, the Yanshanian granites around geothermal wells were formed at the late stage of both the Jurassic and Cretaceous. The geochronological data of the granites in the HGF were integrated with the evolution model for plutonism in this study (Figure 19), yielding findings as follows. The Permian two-mica granites (G4 in Figure 2; Figure 19) intruded into the Paleozoic sandstone at the center of the HGF at 253–251 Ma. During the Jurassic, two magmatic events occurred. At 176.7 Ma, granodiorites were emplaced in the southeast of this study area (Jurassic stage 1), while the intrusion of biotite granites (G3 and G6 in Figure 2; Figure 19) occurred at 155.8–153 Ma (Jurassic stage 2). During the Cretaceous, three stages of magmatism occurred: 1) stage 1: biotite granites (G1) were exposed in the northwest of the HGF, with ages ranging from 143.6 to 140.9 Ma; 2) stage 2: biotite granites (G1) were in intrusive contact with granodiorites (G5) in the southeast of the HGF; 3) stage 3: biotite granite intruded under the two-mica granites and Paleozoic sandstones at 135–135.3 Ma as the reservoir rocks of geothermal resources in the HGF.

7 Conclusion

(1) In the HGF, igneous rocks are dominated by Yanshanian granites (highly fractionated I-type granites), with Permian granites exposed in only limited areas.
(2) As indicated by the Hf isotopic composition of zircons, the reservoir granites (1,500–300 m) originated from the Meso-to Paleo-Proterozoic lower crustal materials.
(3) The heat generated from Cretaceous granites with high heat production serves as a primary heat source for the formation of geothermal energy in the HGF.

Data availability statement

The original contributions presented in the study are included in the article/Supplementary material, further inquiries can be directed to the corresponding author.

Author contributions

YL: Conceptualization, Data curation, Formal Analysis, Investigation, Methodology, Software, Visualization, Writing–original draft, Writing–review and editing. GW: Conceptualization, Funding acquisition, Project administration, Resources, Validation, Writing–review and editing. YX: Funding acquisition, Project administration, Writing–review and editing. HG: Resources, Writing–review and editing. XY: Resources, Writing–review and editing. MY: Data curation, Writing–review and editing. WZ: Resources, Writing–review and editing. ZZ: Investigation, Writing–review and editing.

Funding

The author(s) declare financial support was received for the research, authorship, and/or publication of this article. This work was funded by a project of National Natural Science Foundation of China (41874100), National Key Research and Development

Program of China (2021YFB1507401), China Geological Survey (DD20221676).

Conflict of interest

The authors declare that the research was conducted in the absence of any commercial or financial relationships that could be construed as a potential conflict of interest.

Publisher's note

All claims expressed in this article are solely those of the authors and do not necessarily represent those of their affiliated organizations, or those of the publisher, the editors and the reviewers. Any product that may be evaluated in this article, or claim that may be made by its manufacturer, is not guaranteed or endorsed by the publisher.

References

Alqahtani, F., Aboud, E., Ehsan, M., Naseer, Z., Abdulfarraj, M., Abdelwahed, M. F., et al. (2023a). Geothermal exploration using remote sensing, surface temperature, and geophysical data in lunayyir volcanic field, Saudi Arabia. *Sustainability* 15, 7645. doi:10.3390/su15097645

Alqahtani, F., Ehsan, M., Aboud, E., Abdulfarraj, M., and El-Masry, N. (2023b). Integrated approach using petrophysical, gravity, and magnetic data to evaluate the geothermal resources at the rahat volcanic field, Saudi Arabia. *Front. Earth Sci.* 11, 1135635. doi:10.3389/feart.2023.1135635

Artemieva, I. M., and Thybo, H. (2013). Eunaseis: a seismic model for moho and crustal structure in europe, Greenland, and the north atlantic region. *Tectonophysics* 609, 97–153. doi:10.1016/j.tecto.2013.08.004

Artemieva, I. M., Thybo, H., Jakobsen, K., Sorensen, N. K., and Nielsen, L. S. K. (2017). Heat production in granitic rocks: global analysis based on a new data compilation granite2017. *Earth-Science Rev.* 172, 1–26. doi:10.1016/j.earscirev.2017.07.003

Bea, F., Montero, P., Molina, J. F., Scarrow, J. H., Cambeses, A., and Moreno, J. A. (2018). Lu-hf ratios of crustal rocks and their bearing on zircon hf isotope model ages: the effects of accessories. *Chem. Geol.* 484, 179–190. doi:10.1016/j.chemgeo.2017.11.034

Bhattacharya, S., and Janwari, S. (2015). A short review on lu-hf isotope system in zircon: implications for crustal evolution. *J. Indian Inst. Sci.* 95 (2), 147–157. doi:10.1007/s00531-007-0239-2

Black, L. P., Kamo, S. L., Allen, C. M., Aleinikoff, J. N., Davis, D. W., Korsch, R. J., et al. (2003). Temora 1: a new zircon standard for phanerozoic u–pb geochronology. *Chem. Geol.* 200 (1), 155–170. doi:10.1016/s0009-2541(03)00165-7

Breiter, K., and Škoda, R. (2017). Zircon and whole-rock zr/hf ratios as markers of the evolution of granitic magmas: examples from the teplice caldera (Czech republic/germany). *Mineralogy Petrology* 111 (115), 435–457. doi:10.1007/s00710-017-0509-z

Cai, Y., Liu, H., Feng, Z., Zhou, Y., Liu, X., Wang, Z., et al. (2020). Neoproterozoic active margin of the sw south China block: constraints from u pb ages, sr nd isotopes and geochemical data for the gabbro and granodiorite along the ailaoshan tectonic belt. *Lithos* 358-359, 105387. doi:10.1016/j.lithos.2020.105387

Chappell, B. W., Bryant, C. J., and Wyborn, D. (2012). Peraluminous i-type granites. *Lithos* 153, 142–153. doi:10.1016/j.lithos.2012.07.008

Chappell, B. W., Sial, A. N., Stephens, W. E., and Ferreira, V. P. (1999). Aluminium saturation in i- and s-type granites and the characterization of fractionated haplogranites. *Lithos* 46 (3), 535–551. doi:10.1016/s0024-4937(98)00086-3

Chappell, B. W., and White, A. J. R. (2001). Two contrasting granite types: 25 years later. *Aust. J. Earth Sci.* 48 (4), 489–499. doi:10.1046/j.1440-0952.2001.00882.x

Chen, C. H., Lee, C. Y., and Shinjo, R. I. (2008). Was there jurassic paleo-pacific subduction in south China? constraints from 40ar/39ar dating, elemental and sr-nd-pb isotopic geochemistry of the mesozoic basalts. *Lithos* 106 (1-2), 83–92. doi:10.1016/j.lithos.2008.06.009

Chen, H., Song, R., Zhaong, C., Liang, Y., Wang, Y., Zheng, F., et al. (2023). Geothermal storage evaluation of geothermal resources in hot dry rock based on factor analysis method. *J. Chengdu Univ. Technol. Sci. Technol. Ed.* 50 (03), 333–350. doi:10.3969/j.issn.1671-9727.2023.03.08

Chen, X., Liu, J., Zhang, Q., Yang, Z., Yang, L., and Wu, J. (2014). Characteristics of hf isotopes and zircon u-pb ages of granites in the cuihongshan iron polymetallic deposit, heilongjiang and their geologic implications. *Bull. Mineralogy Petrology Geochem.* 33 (5), 636–644. doi:10.1002/gj.3224

Collins, W. J., Beams, S. D., White, A. J. R., and Chappell, B. W. (1982). Nature and origin of a-type granites with particular reference to southeastern Australia. *Contributions Mineralogy Petrology* 80 (2), 189–200. doi:10.1007/bf00374895

Ferry, J. M., and Watson, E. B. (2007). New thermodynamic models and revised calibrations for the ti-in-zircon and zr-in-rutile thermometers. *Contributions Mineralogy Petrology* 154 (4), 429–437. doi:10.1007/s00410-007-0201-0

Geng, J., Li, H., Zhang, J., Zhou, H., and Li, H. (2011). Zircon hf isotope analysis by means of la-mc-icp-ms. *Geol. Bull. China* 30 (10), 1508–1513.

Hasterok, D., and Chapman, D. S. (2011). Heat production and geotherms for the continental lithosphere. *Earth Planet. Sci. Lett.* 307 (1-2), 59–70. doi:10.1016/j.epsl.2011.04.034

Hu, R. Z., Chen, W. T., Xu, D. R., and Zhou, M. F. (2017). Reviews and new metallogenic models of mineral deposits in south China: an introduction. *J. Asian Earth Sci.* 137, 1–8. doi:10.1016/j.jseaes.2017.02.035

Kemp, A. I. S., and Hawkesworth, C. J. (2003). 3.11 – granitic perspectives on the generation and secular evolution of the continental crust. *Treatise Geochem.* 3 (6), 349–410. doi:10.1016/j.epsl.2009.05.011

Kromkhun, K. (2010). Petrogenesis of high heat producing granite: implication for mt painter province, south Australia. Thesis. Adelaide: University of Adelaide, School of Earth and Environmental Sciences.

Li, T., Lin, W., Gan, H., Yue, G., Zhang, D., and Wang, G. (2020a). Ocurence prospect of hdr and target site selection study in southeastern of China. *Acta Geol. Sinca* 026 (002), 187–200.

Li, T., Lin, W., Gan, H., Yue, G., Zhang, D., and Wang, G. (2020b). Research on the genetic model and exploration progress of hot dry rock resources on the southeast coast of China. *J. Geomechanics* 026 (002), 187–200. doi:10.12090/j.issn.1006-6616.2020.26.02.018

Li, X. H., Li, W. X., Li, Z. X., Lo, C. H., Wang, J., Ye, M. F., et al. (2009). Amalgamation between the yangtze and cathaysia blocks in south China: constraints from shrimp u–pb zircon ages, geochemistry and nd–hf isotopes of the shuangxiwu volcanic rocks. *Precambrian Res.* 174 (1), 117–128. doi:10.1016/j.precamres.2009.07.004

Li, Z.-X., and Li, X.-H. (2007). Formation of the 1300-km-wide intracontinental orogen and postorogenic magmatic province in mesozoic south China: a flat-slab subduction model. *Geology* 35 (2), 179–182. doi:10.1130/g23193a.1

Liao, Y., Zhang, D., Danyushevsky, L. V., Li, T., and Liu, Y. (2021). Protracted lifespan of the late mesozoic multistage qianlishan granite complex, nanling range, se China: implications for its genetic relationship with mineralization in the dongpo ore field. *Ore Geol. Rev.* 139, 104445. doi:10.1016/j.oregeorev.2021.104445

Lin, W., Gan, H., Wang, G., and Ma, F. (2016). Occurrence prospect of hdr and target site selection study in southeastern of China. *Acta Geol. Sin.* 90 (08), 2043–2058.

Lin, W., Wang, G., and Gan, H. (2023). Differential crustal thermal structure and geothermal significance in the igneous region of southeastern China. *Acta Geol. Sin.* 2023, 1–14. doi:10.19762/j.cnki.dizhixuebao.2023027

Lin, W., Wang, G., Gan, H., Wang, A., Yue, G., Long, X., et al. (2022). Heat generation and accumulation for hot dry rock resources in the igneous rock distribution areas of southeastern China. *Lithosphere* 2021 (5), 2039112. doi:10.2113/2022/2039112

Liu, C., Zheng, J., Li, Z., Li, Y., Hao, Q., and Li, J. (2021). Analysis on the situation and countermeasures of water resources supply and demand in the cities of small and medium-sized river basins along southeast coast of China — taking xiamen city as an example. *J. Groundw. Sci. Eng.* 9 (4), 350. doi:10.19637/j.cnki.2305-7068.2021.04.008

Liu, H., Guo, H., Xing, L., Zhan, Y., Li, F., Shao, J., et al. (2016). Geochemical behaviors of rare earth elements in groundwater along a flow path in the north China plain. *J. Asian Earth Sci.* 117 (MAR.1), 33–51. doi:10.1016/j.jseaes.2015.11.021

Liu, Y. S., Gao, S., Hu, Z. C., Gao, C. G., Zong, K. Q., and Wang, D. B. (2010). Continental and oceanic crust recycling-induced melt-peridotite interactions in the trans-north China orogen: U-pb dating, hf isotopes and trace elements in zircons from mantle xenoliths. *J. Petrology* 51 (1-2), 537–571. doi:10.1093/petrology/egp082

Lu, S. M. (2018). A global review of enhanced geothermal system (egs). *Renew. Sustain. Energy Rev.* 81, 2902–2921. doi:10.1016/j.rser.2017.06.097

Lund, J. W., and Toth, A. N. (2021). Direct utilization of geothermal energy 2020 worldwide review. *Geothermics* 90, 101915. doi:10.1016/j.geothermics.2020.101915

Lv, Q. (2010). Methods for chemical analysis of silicate rocks - part 28: Determination of 16 major and minor elements content (gb/t 14506.28-2010). Beijing; General Administration of Quality Supervision, Inspection and Quarantine of the People's Republic of China.

Ma, F., Wang, G., Sun, H., and Sun, Z. (2022). Indication of hydrogen and oxygen stable isotopes on the characteristics and circulation patterns of medium-low temperature geothermal resources in the guanzhong basin, China. *J. Groundw. Sci. Eng.* 10 (1), 70. doi:10.19637/j.cnki.2305-7068.2022.01.007

Mao, J. W., Chen, M. H., Yuan, S. D., and Guo, C. L. (2011). Geological characteristics of the qinhang (or shihang) metallogenic belt in south China and spatial-temporal distribution regularity of mineral deposits. *Acta Geol. Sin.* 85 (5), 636–658.

Marshall, V. J. (2014). Petrological, geochemical and geochronological characterisation of heat-producing granites. Heat Producing Granite.

Mclaren, S., Neumann, N., Sandiford, M., and Wyborn, L. (1999). Post-intrusion heating associated with high-heat-producing proterozoic granites implications for mineralisation?: AGSO Research Newsletter, 30–31.

Pang, Z., Huang, T., Tian, J., Cheng, Y., Huang, T., et al. (2023). Formation of the hydrothermal system from granite reservoir for power generation in igneous rock areas of south China. *Geothermics* 110, 102673. doi:10.1016/j.geothermics.2023.102673

Paton, C., Woodhead, J. D., Hellstrom, J. C., Hergt, J. M., Greig, A., and Maas, R. (2010). Improved laser ablation u-pb zircon geochronology through robust downhole fractionation correction. *Geochem. Geophys. Geosystems* 11 (3). doi:10.1029/2009gc002618

Pearce, J. A., Harris, N. B. W., and Tindle, A. G. (1984). Trace-element discrimination diagrams for the tectonic interpretation of granitic-rocks. *J. Petrology* 25 (4), 956–983. doi:10.1093/petrology/25.4.956

Qiu, X. L., Wang, Y., Wang, Z. Z., Regenauer-Lieb, K., Zhang, K., and Liu, J. (2018). Determining the origin, circulation path and residence time of geothermal groundwater using multiple isotopic techniques in the heyuan fault zone of southern China. *J. Hydrology* 567, 339–350. doi:10.1016/j.jhydrol.2018.10.010

Qiu, Z., Yan, Q., Li, S., Wang, H., Tong, L., Zhang, R., et al. (2017). Highly fractionated early cretaceous i-type granites and related sn polymetallic mineralization in the jinkeng deposit, eastern guangdong, se China: constraints from geochronology, geochemistry, and hf isotopes. *Ore Geol. Rev.* 88, 718–738. doi:10.1016/j.oregeorev.2016.10.008

Roth, J., and Littke, R. (2022). Down under and under cover-the tectonic and thermal history of the cooper and central eromanga basins (central eastern Australia). *Geosciences* 12 (3), 117. doi:10.3390/geosciences12030117

Sláma, J., Košler, J., Condon, D. J., Crowley, J. L., Gerdes, A., Hanchar, J. M., et al. (2008). Plešovice zircon—a new natural reference material for u–pb and hf isotopic microanalysis. *Chem. Geol.* 249 (1-2), 1–35. doi:10.1016/j.chemgeo.2007.11.005

Stepanov, A. S., Meffre, S., Mavrogenes, J., and Steadman, J. (2016). Nb-ta fractionation in peraluminous granites: a marker of the magmatichydrothermal transition. *Geology* 44, 231–234. doi:10.1130/G37475.1

Sun, S.-S., and Mcdonough, W.-S. (1989). Chemical and isotopic systematics of oceanic basalts: implications for mantle composition and processes. *Geol. Soc. Lond. Spec. Publ.* 42 (1), 313–345. doi:10.1144/gsl.sp.1989.042.01.19

Tester, J. W., Anderson, B. J., Batchelor, A. S., Blackwell, D. D., Dipippo, R., and Drake, E. M. (2006). *The future of geothermal energy*. Idaho Falls: Massachusetts Institute of Technology.

Ullah, J., Li, H., Ashraf, U., Heping, P., Ali, M., Ehsan, M., et al. (2023). Knowledge-based machine learning for mineral classification in a complex tectonic regime of yingxiu-beichuan fault zone, sichuan basin. *Geoenergy Sci. Eng.* 229, 212077. doi:10.1016/j.geoen.2023.212077

Wang, Y., Furlong, K., Fuchs, S., He, L., and Hu, S. (2023). Terrestrial heat flow variation with depth caused by anomalously high radiogenic heat production. *Geophys. Res. Lett.* 50 (8), e2022GL102312. doi:10.1029/2022GL102312

Whalen, J. B., Currie, K. L., and Chappell, B. W. (1987). A-type granites: geochemical characteristics, discrimination and petrogenesis. *Contributions Mineralogy Petrology* 95 (4), 407–419. doi:10.1007/bf00402202

Wiedenbeck, M., Allé, P., Corfu, F., Griffin, W. L., Meier, M., Oberli, F., et al. (1995). Three natural zircon standards for u-th-pb, lu-hf, trace element and ree analyses.

Wyborn, D., Chappell, B. W., and James, M. (2001). Examples of convective fractionation in high-temperature granites from the lachlan fold belt. *Aust. J. Earth Sci.* 48 (4), 531–541. doi:10.1046/j.1440-0952.2001.00877.x

Xi, Y., Zhao, Y., and Da, Y. (2021). Geothermal structure revealed by curie isothermal surface under guangdong province, China. *J. Groundw. Sci. Eng.* 9 (2), 114. doi:10.19637/j.cnki.2305-7068.2021.02.003

Xiao, Z., Wang, S., Qi, S., Kuang, J., Han, Y., Tian, F., et al. (2019). Petrogenesis, tectonic evolution and geothermal implications of mesozoic granites in the huangshadong geothermal field, south China. *J. Earth Sci.* 31 (3), 141–158. doi:10.1007/s12583-019-1242-9

Zhang, C., Feng, Q., Zhang, L., Qin, S., Jiang, G., Hu, J., et al. (2022). Characteristics of radiogenic heat production of widely distributed granitoids in western sichuan, southeast Tibetan plateau. *Lithosphere* 2022, 4165618. doi:10.2113/2022/4165618

Zhang, Y., Yang, J. H., Sun, J. F., Zhang, J. H., Chen, J. Y., and Li, X. H. (2015). Petrogenesis of jurassic fractionated i-type granites in southeast China: constraints from whole-rock geochemical and zircon u-pb and hf-o isotopes. *J. Asian Earth Sci.* 111, 268–283. doi:10.1016/j.jseaes.2015.07.009

Zhang, Z. J., Badal, J., Li, Y. K., Chen, Y., Yang, L. Q., and Teng, J. W. (2005). Crust-upper mantle seismic velocity structure across southeastern China. *Tectonophysics* 395 (1-2), 137–157. doi:10.1016/j.tecto.2004.08.008

Zhang, Z. J., Xu, T., Zhao, B., and Badal, J. (2013). Systematic variations in seismic velocity and reflection in the crust of cathaysia: new constraints on intraplate orogeny in the south China continent. *Gondwana Res.* 24 (3-4), 902–917. doi:10.1016/j.gr.2012.05.018

Zhao, P., and Luo, D. (1995). Characteristics of heat production distribution in se China. *Acta Petrol. Sin.* 11 (3), 292–305.

Zhou, X. M., Sun, T., Shen, W. Z., Shu, L. S., and Niu, Y. L. (2006). Petrogenesis of mesozoic granitoids and volcanic rocks in south China: a response to tectonic evolution. *Episodes* 29 (1), 26–33. doi:10.18814/epiiugs/2006/v29i1/004

Zhou, Y., Sun, S., Feng, Z., Xu, C., Cai, Y., Liang, X., et al. (2021). A new insight into the eastern extension of the proto-tethyan margin of gondwana by early paleozoic volcanic rocks in south China. *Lithos* 398-399, 106328. doi:10.1016/j.lithos.2021.106328

Zuo, Q., Ye, T., Feng, Y., Ge, Z., and Wang, Y. (2018). Spatial database of serial suite-tectonic map-sheets of mainland China (1: 250, 000). *Geol. China* 45 (S1), 1–26. doi:10.12029/gc2018Z101